

# Stoichiometry-Controlled $\text{Mo}_x\text{W}_{1-x}\text{Te}_2$ Nanowhiskers: A Novel Electrocatalyst for Pt-Free Dye-Sensitized Solar Cells

Roshan Jesus Mathew,<sup>□</sup> Chuan-Pei Lee,<sup>□</sup> Chi-Ang Tseng, Pradyumna Kumar Chand, Yi-June Huang, Han-Ting Chen, Kuo-Chuan Ho, Aswin kumar Anbalagan, Chih-Hao Lee, and Yit-Tsong Chen\*



Cite This: *ACS Appl. Mater. Interfaces* 2020, 12, 34815–34824



Read Online

ACCESS |



Metrics & More



Article Recommendations



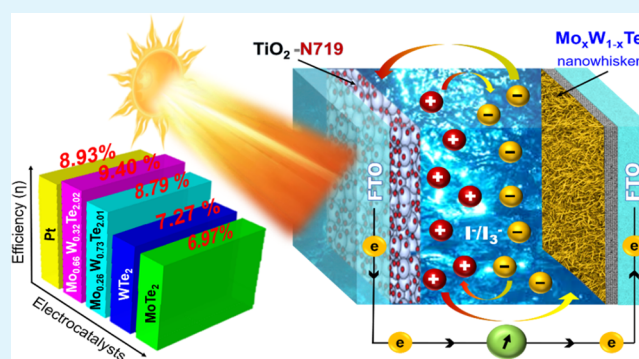
Supporting Information

**ABSTRACT:** Novel polymorphic  $\text{Mo}_x\text{W}_{1-x}\text{Te}_2$ -based counter electrodes possess high carrier mobility, phase-dependent lattice distortion, and surface charge density wave to boost the charge-transfer kinetics and electrocatalytic activity in dye-sensitized solar cells (DSSCs). Here, we report the syntheses of stoichiometry-controlled binary and ternary  $\text{Mo}_x\text{W}_{1-x}\text{Te}_2$  nanowhiskers directly on carbon cloth (CC), denoted by  $\text{Mo}_x\text{W}_{1-x}\text{Te}_2/\text{CC}$ , with an atmospheric chemical vapor deposition technique. The synthesized  $\text{Mo}_x\text{W}_{1-x}\text{Te}_2/\text{CC}$  samples, including  $1T'$ - $\text{MoTe}_2/\text{CC}$ ,  $T_d$ - $\text{WTe}_2/\text{CC}$ ,  $T_d$ - $\text{Mo}_{0.26}\text{W}_{0.73}\text{Te}_{2.01}/\text{CC}$ , and  $1T'$ - &  $T_d$ - $\text{Mo}_{0.66}\text{W}_{0.32}\text{Te}_{2.02}/\text{CC}$ , were then employed as different counter electrodes to study their electrochemical activities and efficiencies in DSSCs. The photovoltaic parameter analysis manifests that  $\text{Mo}_x\text{W}_{1-x}\text{Te}_2/\text{CC}$ s are more stable than a standard Pt/CC in the  $\Gamma/I_3^-$  electrolyte examined by cyclic voltammetry over 100 cycles. A  $1T'$ - &  $T_d$ - $\text{Mo}_{0.66}\text{W}_{0.32}\text{Te}_{2.02}/\text{CC}$ -based DSSC can achieve a photocurrent density of  $16.29 \text{ mA cm}^{-2}$ , a maximum incident photon-to-electron conversion efficiency of 90% at 550 nm excitation, and an efficiency of 9.40%, as compared with 8.93% of the Pt/CC counterpart. Moreover, the  $1T'$ - &  $T_d$ - $\text{Mo}_{0.66}\text{W}_{0.32}\text{Te}_{2.02}/\text{CC}$  shows lower charge-transfer resistance ( $0.62 \Omega \text{ cm}^2$ ) than a standard Pt/CC ( $1.19 \Omega \text{ cm}^2$ ) in electrocatalytic reactions. Notably,  $\text{Mo}_x\text{W}_{1-x}\text{Te}_2$  nanowhiskers act as an electron expressway by shortening the path of carrier transportation in the axial direction from a counter electrode to electrolytic ions to enhance the reaction kinetics in DSSCs. This work demonstrates that the nanowhisker-structured  $1T'$ - &  $T_d$ - $\text{Mo}_{0.66}\text{W}_{0.32}\text{Te}_{2.02}/\text{CC}$  with high carrier mobility and robust surface states can serve as a highly efficient counter electrode in DSSCs to replace the conventional Pt counter electrode for electrocatalytic applications.

**KEYWORDS:** chemical vapor deposition,  $\text{Mo}_x\text{W}_{1-x}\text{Te}_2$ , dye-sensitized solar cells, counter electrodes, electrocatalysis

## INTRODUCTION

The development of dye-sensitized solar cells (DSSCs) has revolutionized the third-generation photovoltaic technology by achieving efficient solar-energy conversion, low-cost large-scale processing, and facile fabrication methodology.<sup>1,2</sup> Despite the rise of various highly efficient architectures for solar cells,<sup>3–6</sup> a large scale of research has been conducted for boosting the efficiency of DSSCs with durable and low-cost novel functional materials.<sup>7–12</sup> In DSSCs, a counter electrode (CE) is crucial and has a vital influence on the photovoltaic performance. A competent CE should have eminent electrical conductivity, large surface area, excellent electrocatalytic activity, and reliable electrochemical and mechanical stabilities.<sup>13–15</sup> Platinum (Pt) is a popular CE material for DSSCs;<sup>16</sup> however, its scarcity and expensiveness have sparked research for other alternative sources. Up to now, a wide range of electrocatalytic materials has been explored for electrocatalytic applications,<sup>17–21</sup> including the transition metal dichalcogenides (TMDs) of  $\text{MX}_2$  ( $M = \text{Mo}$  or  $\text{W}$  and  $X = \text{S}$ ,  $\text{Se}$ ,  $\text{Te}$ , etc.).<sup>22–26</sup> These two-



dimensional (2D) TMDs of strong intralayer covalent bonds and weak interlayer van der Waals interaction<sup>27</sup> possess excellent electrical conductivity and large surface area, which are ideal candidates to be used as CEs in DSSC devices.<sup>28</sup>

For TMD-based electrocatalysts to assist the redox reactions in DSSCs, a constant electron supply on the TMD surface can benefit electrochemical activity significantly. Among various TMD crystals, although the metallic  $1T$  phase is unstable and could make an easy transition into the semiconducting  $2H$  phase, the  $1T$  phase exhibits better electrocatalytic activity than the  $2H$  phase because the high carrier mobility in the metallic  $1T$  materials reduces the energy loss during redox

Received: April 17, 2020

Accepted: July 13, 2020

Published: July 13, 2020



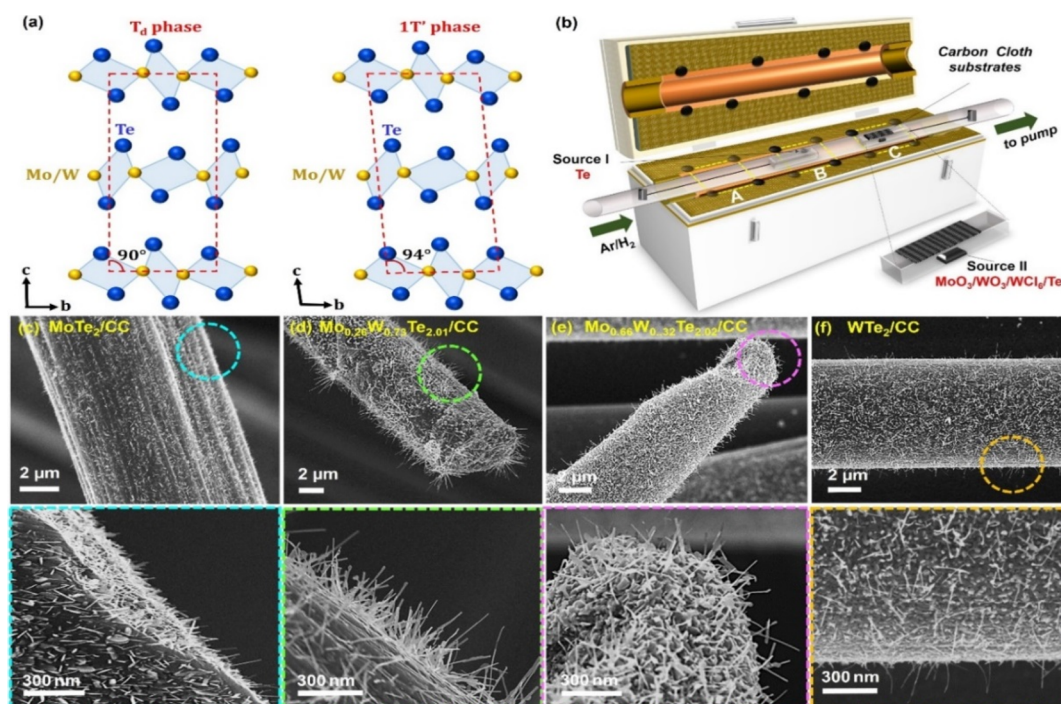


**Figure 1.** (a) A layered structure of the  $\text{Mo}_x\text{W}_{1-x}\text{Te}_2$  crystal possesses the  $T_d$  or  $1T'$  phase in which the red dotted box indicates a unit cell. (b) APCVD experimental setup for the growth of  $\text{Mo}_x\text{W}_{1-x}\text{Te}_2$  nanowiskers is represented. The SEM images of (c)  $\text{MoTe}_2$ , (d)  $\text{Mo}_{0.26}\text{W}_{0.73}\text{Te}_{2.01}$ , (e)  $\text{Mo}_{0.66}\text{W}_{0.32}\text{Te}_{2.02}$ , and (f)  $\text{WTe}_2$  nanowiskers decorated on CC substrates are presented. The detailed structures of  $\text{Mo}_x\text{W}_{1-x}\text{Te}_2$  nanowiskers on a CC fiber, marked by the dashed circles in the top panels, are highlighted in the bottom panels.

reactions.<sup>29,30</sup> Nevertheless, recent studies predicted that Weyl semi-metals (WSMs) hold high carrier mobility<sup>31,32</sup> and can be an excellent candidate for electrocatalysts where the WSM surfaces containing robust topological states can act as long-term stable catalytic planes.<sup>30,33,34</sup> In WSMs, the valence and conduction bands cross near the Fermi energy level, called Weyl points, which can enhance carrier mobility and exhibit robust metallic surface states.<sup>32,35</sup> In the electrocatalytic processes of DSSCs, a dense flow of electrons and holes is favorable for redox reactions. In addition, the high mobilities of charge carriers can not only accelerate charge transfers to enhance reaction kinetics at the CE but also reduce electron–hole recombinations at the photoanode by the rapid separation of electron–hole pairs.<sup>32</sup> Moreover, the topological states of a WSM protect the semi-metallic surface from contamination, which is one of the significant challenges encountered in electrocatalysis.<sup>36</sup>

Among WSMs, both  $\text{MoTe}_2$  and  $\text{WTe}_2$  of various crystal phases, thicknesses, and morphologies have shown their catalytic abilities in electrochemical applications.<sup>35–40</sup> Interestingly, the  $\text{Mo}_x\text{W}_{1-x}\text{Te}_2$  alloys by doping Mo into the  $\text{WTe}_2$  crystal were theoretically predicted<sup>41</sup> and spectroscopically proven<sup>42</sup> to be able to possess polymorphic WSMs and tunable topological surface states. The structures of Te-based compounds exhibit polymorphism with diverse electronic properties in different crystal phases, including the  $2H$  semiconductor (hexagonal, space group  $P6_3/mmc$ ),  $1T'$  semi-metal (monoclinic, space group  $P2_1/m$ ), and  $T_d$  semi-metal (orthorhombic, space group  $Pmn2_1$ ).<sup>42–44</sup> Based on theoretical, crystallographic, and spectroscopic analyses, the stoichiometry-dependent  $\text{Mo}_x\text{W}_{1-x}\text{Te}_2$  crystal exhibits the  $1T'$  phase at  $x \geq 0.96$  and the  $T_d$  phase at  $x \leq 0.37$  (Figure 1a) but a mixture of  $1T' + T_d$  phases for the intermediate compositions of  $0.37 < x < 0.96$ .<sup>42,45</sup> It is noted that  $1T'$ - $\text{Mo}_x\text{W}_{1-x}\text{Te}_2$  ( $x \geq$

$0.96$ ) is unstable and easily gives rise to a phase transition to the  $2H$  phase.<sup>41</sup> In our previous work, we demonstrated that semi-metallic  $T_d$ - $\text{Mo}_x\text{W}_{1-x}\text{Te}_2$  nanosheets hold high carrier mobility and act as efficient electrocatalysts in DSSCs.<sup>46</sup>

To explore the electrochemical activities of this Te-based alloy system, we fabricated one-dimensional (1D) binary and ternary  $\text{Mo}_x\text{W}_{1-x}\text{Te}_2$  nanowiskers with semi-metallic  $1T'$  or  $T_d$  phase and made comparative analysis for their catalytic efficiencies in electrochemical reactions. Notably, 1D nanostructures not only enhance the carrier collection ability by exposing more active sites than 2D-layered structures but also act as an electron expressway by shortening the path of carrier transportation in the axial direction.<sup>47–49</sup> In this work, we synthesized stoichiometry-controlled  $\text{Mo}_x\text{W}_{1-x}\text{Te}_2$  nanowiskers, which were further employed as competent electrocatalytic CEs in a Pt-free DSSC. We established an atmospheric chemical vapor deposition (APCVD) system to grow stoichiometry-controlled  $\text{Mo}_x\text{W}_{1-x}\text{Te}_2$  nanowiskers directly on carbon cloth (CC) substrates (denoted by  $\text{Mo}_x\text{W}_{1-x}\text{Te}_2/\text{CC}$ ). We then conducted the structural characterization and compositional analysis for the as-grown  $\text{Mo}_x\text{W}_{1-x}\text{Te}_2$  nanowiskers followed by employing these  $\text{Mo}_x\text{W}_{1-x}\text{Te}_2/\text{CC}$ s as CEs in a DSSC to investigate their electrocatalytic performance. From our studies, the stoichiometry-tuned  $\text{Mo}_x\text{W}_{1-x}\text{Te}_2$  nanowisker-based CEs exhibited the minimal charge-transfer resistance and enhanced the power conversion efficiency of 9.4%, comparable to a standard Pt CE under the same experimental conditions.

## EXPERIMENTAL METHODS

**Synthesis of  $\text{Mo}_x\text{W}_{1-x}\text{Te}_2$  Nanowiskers.** An APCVD system, equipped with a three-zone tube furnace (Thermocraft Inc. Winston N.C, USA) and a 1" quartz tube, was utilized to synthesize  $\text{Mo}_x\text{W}_{1-x}\text{Te}_2/\text{CC}$ . Before the APCVD reactions, CC was soaked

into a 95–97% H<sub>2</sub>SO<sub>4</sub> solution for 1 week and then washed with deionized water, ethanol, and isopropanol sequentially. The CC substrates on a ceramic boat were loaded into the quartz tube and placed downstream in the APCVD furnace. The ceramic boat contained the chemical precursors with an adjustable stoichiometric (molar) ratio between MoO<sub>3</sub> and a mixture of WO<sub>3</sub>, WCl<sub>6</sub>, and Te with the weight ratio of 1:1:1 (source I). In the quartz tube, an excess of 200 mg Te powder (source II) was placed upstream relative to the mixture of chemical precursors. After the quartz tube was flushed with Ar twice, the reaction chamber was evacuated to 20 mTorr and then filled with Ar (at 50 sccm) to 760 Torr. While heating source I to 825 °C, source II was heated to 550 °C and H<sub>2</sub> (at 7 sccm) was introduced at 760 °C to assist the reduction of the metal oxides. After the growth of nanowhiskers for 15 min, the H<sub>2</sub> supply was turned off followed by an Ar flow (600 sccm). Meanwhile, the rapid cooling of the substrates was performed by drawing the growth substrate quickly out of the hot zone of the furnace with the assistance of a magnet. The as-synthesized samples were kept in vacuum for further structural characterizations. The Mo<sub>x</sub>W<sub>1-x</sub>Te<sub>2</sub> nanowhiskers of different composition ratios were synthesized following the same procedures by changing the stoichiometric ratios of the alloys.

**Structural Characterizations.** Surface morphology and elemental mapping of the as-grown Mo<sub>x</sub>W<sub>1-x</sub>Te<sub>2</sub> nanowhiskers were conducted in a scanning electron microscope (Jeol JSM-7800F) with an energy-dispersive spectroscopy (EDS) detector. The X-ray diffraction (XRD) experiments at  $\lambda = 0.1377$  nm were carried out with the beamline BL17B at the Taiwan light source, National Synchrotron Radiation Research Center (NSRRC) Facility, Taiwan. X-ray photoelectron spectroscopy (XPS) was performed using an ESCA spectrometer (VG Scientific, Escalab 250) equipped with a monochromatic X-ray source (1486.6 eV Al K $\alpha$ ) and CASA XPS software (v.2.3.17, Casa Software Ltd., Wilmslow, U.K.) was used to analyze the spectra. The binding energies of the observed signals were calibrated against the carbon C 1s peak at 284.8 eV. The Shirley–Sherwood method was employed to subtract the background. Raman spectra were acquired in a microRaman spectrometer (Horiba, LabRAM HR Evolution), including an optical microscope (Olympus, CX41), a grating of 1800 grooves/mm, a detector (Jobin Won Horiba, SDrive-500 Syncernity), and a 532 nm laser for excitation. Frequency calibration of the observed Raman signals was assisted by the peak of Si at 520 cm<sup>-1</sup>. High-resolution transmission electron microscopy (HR-TEM) was conducted in a transmission electron microscope (JEOL, JEM-2100F) with an operating voltage of 200 kV.

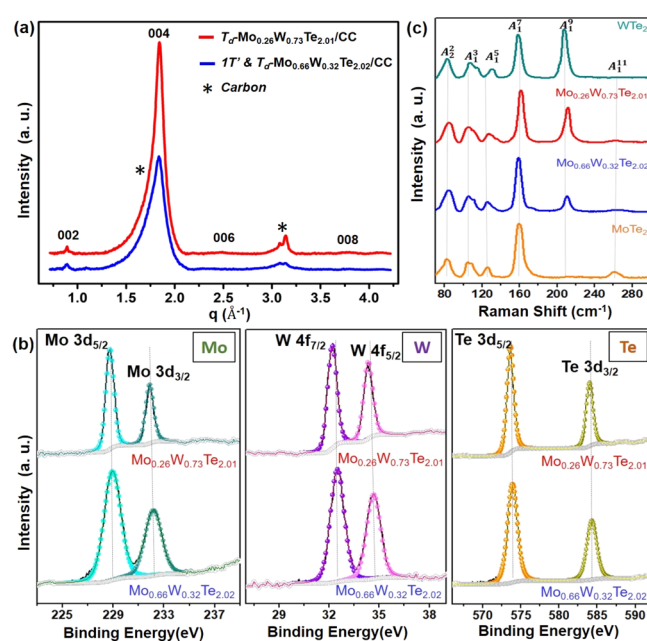
**DSSC Fabrication.** A cleaned fluorine-doped SnO<sub>2</sub> (FTO) conducting glass substrate (TEC-7, 10  $\Omega$  sq<sup>-1</sup>, NSG America), a scattering layer ( $\sim 4$   $\mu$ m in thickness), a transparent layer ( $\sim 10$   $\mu$ m in thickness), and a compact layer ( $\sim 100$  nm in thickness) of TiO<sub>2</sub> were used as the photoanode. Each TiO<sub>2</sub> layer was sintered at 500 °C for 30 min under an ambient condition. The TiO<sub>2</sub> electrode was then immersed in a dye solution (500  $\mu$ M N719 in a mixed solvent of acetonitrile and tert-butyl alcohol with the volume ratio of 1:1) for 24 h. The as-prepared dye-sensitized TiO<sub>2</sub> photoanode and a CE were used to fabricate the DSSC device with a cell gap of 60  $\mu$ m by using a Surlyn film as the spacer (Solaronix S.A., Switzerland). The electrolyte used for DSSC measurements contained 0.5 M 4-tert-butylpyridine (TBP), guanidine thiocyanate (GuSCN), 0.35 M I<sub>2</sub>, 0.1 M, and 1.2 M 1,2-dimethyl-3-propylimidazolium iodide (DMPII) in 3-methoxypropionitrile (MPN)/acetonitrile (ACN) (with the volume ratio of 8:2).

## RESULTS AND DISCUSSION

A three-zone tube furnace was employed to synthesize stoichiometry-controlled Mo<sub>x</sub>W<sub>1-x</sub>Te<sub>2</sub> nanowhiskers by properly selecting the stoichiometric ratios of chemical precursors. The ternary Mo<sub>x</sub>W<sub>1-x</sub>Te<sub>2</sub> nanowhiskers were grown at 820 °C on a CC substrate followed by rapid cooling after the growth at a rate of 90 °C min<sup>-1</sup> to preserve the crystal phase formed during the APCVD reaction (especially to prevent the phase transition from 1T' to 2H). The APCVD system used for the

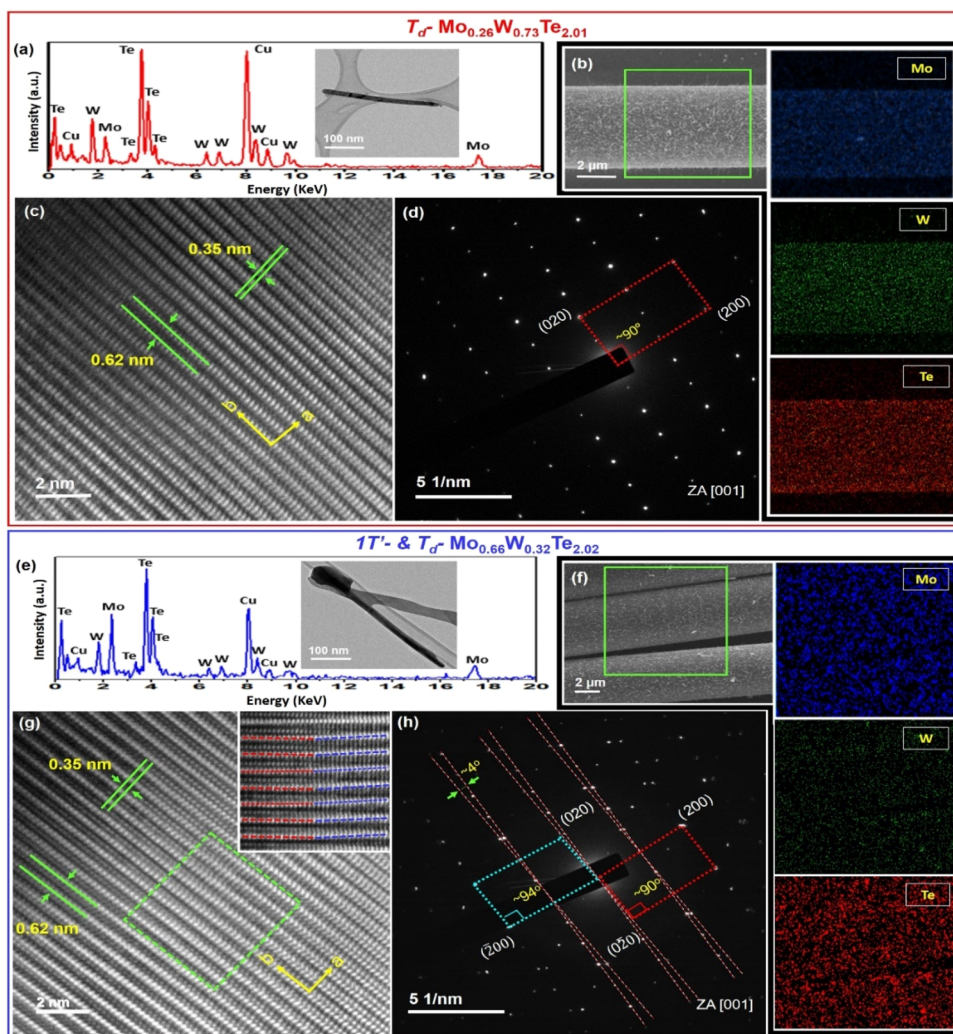
growth of Mo<sub>x</sub>W<sub>1-x</sub>Te<sub>2</sub> nanowhiskers is illustrated in Figure 1B with the synthesis procedures for different stoichiometric ratios given in Experimental Methods and Section S1 of the Supporting Information. The detailed chemical processes of growing Mo<sub>x</sub>W<sub>1-x</sub>Te<sub>2</sub> crystals in the APCVD reactions can be found in our earlier publication.<sup>50</sup> With this synthetic method, Mo<sub>x</sub>W<sub>1-x</sub>Te<sub>2</sub> nanowhiskers were grown on carbon fibers (Figure S2a–f of Section S2 of the Supporting Information). The formation of nanowhiskers could have followed the self-catalyzing vapor–solid–solid (VSS) model,<sup>51–53</sup> but the growth mechanism needs further investigation. Shown in Figure 1c–f are the SEM images of the as-grown Mo<sub>x</sub>W<sub>1-x</sub>Te<sub>2</sub> nanowhiskers with four different stoichiometric ratios ( $x = 0, 0.26, 0.66, \text{ and } 1$ ) where Mo<sub>x</sub>W<sub>1-x</sub>Te<sub>2</sub> nanowhiskers of  $\sim 400$  nm in length were grown densely on CC fibers (also see Figure S2a–c of the Supporting Information).

Figure 2a shows the energy-independent synchrotron XRD spectra of T<sub>d</sub>-Mo<sub>0.26</sub>W<sub>0.73</sub>Te<sub>2</sub>/CC and 1T' & T<sub>d</sub>-Mo<sub>0.66</sub>W<sub>0.32</sub>Te<sub>2</sub>/CC



**Figure 2.** (a) The observed synchrotron XRD spectra of T<sub>d</sub>-Mo<sub>0.26</sub>W<sub>0.73</sub>Te<sub>2.01</sub>/CC (red) and 1T' & T<sub>d</sub>-Mo<sub>0.66</sub>W<sub>0.32</sub>Te<sub>2.02</sub> (blue) were analyzed to obtain the crystalline domain sizes of 21.6 and 15.9 nm, respectively. (b) The observed XPS spectra of T<sub>d</sub>-Mo<sub>0.26</sub>W<sub>0.73</sub>Te<sub>2.01</sub> (top traces) and 1T' & T<sub>d</sub>-Mo<sub>0.66</sub>W<sub>0.32</sub>Te<sub>2.02</sub> (bottom traces) exhibit the Mo 3d, W 4f, and Te 3d levels. In T<sub>d</sub>-Mo<sub>0.26</sub>W<sub>0.73</sub>Te<sub>2.01</sub>, the binding energies include 228.69 (3d<sub>5/2</sub>) and 231.85 eV (3d<sub>3/2</sub>) for Mo, 32.19 (4f<sub>7/2</sub>) and 34.33 eV (4f<sub>5/2</sub>) for W, and 573.60 (3d<sub>5/2</sub>) and 583.96 eV (3d<sub>3/2</sub>) for Te. Similarly, in 1T' & T<sub>d</sub>-Mo<sub>0.66</sub>W<sub>0.32</sub>Te<sub>2.02</sub>, the binding energies observed are 228.94 (3d<sub>5/2</sub>) and 232.17 eV (3d<sub>3/2</sub>) for Mo, 32.46 (4f<sub>7/2</sub>) and 34.65 eV (4f<sub>5/2</sub>) for W, and 573.90 (3d<sub>5/2</sub>) and 584.29 eV (3d<sub>3/2</sub>) for Te. (c) Raman spectra of the as-synthesized WTe<sub>2</sub> (green), T<sub>d</sub>-Mo<sub>0.26</sub>W<sub>0.73</sub>Te<sub>2.01</sub> (red), 1T' & T<sub>d</sub>-Mo<sub>0.66</sub>W<sub>0.32</sub>Te<sub>2.02</sub> (blue), and MoTe<sub>2</sub> (orange) nanowhiskers. The vertical grey dotted lines are a guide to the eye for inspecting the spectral shifts of A<sub>2</sub><sup>'</sup>, A<sub>3</sub><sup>'</sup>, A<sub>1</sub><sup>'</sup>, A<sub>1</sub><sup>'</sup> and A<sub>1</sub><sup>''</sup> with respect to MoTe<sub>2</sub> and A<sub>1</sub><sup>'</sup> to WTe<sub>2</sub>.

Mo<sub>0.66</sub>W<sub>0.32</sub>Te<sub>2.02</sub> nanowhiskers plotted in  $q$  space ( $q = \frac{4\pi \sin\theta}{\lambda}$ ) where  $\theta$  is the Bragg's diffraction angle and  $\lambda$  is the wavelength of the X-ray radiation. The data analysis shows the (002), (004), (006), and (008) peaks with a significant reflex along (002), featuring the preferred growth direction of



**Figure 3.** (a–d) Compositional analysis and crystal characterization of  $T_d\text{-Mo}_{0.26}\text{W}_{0.73}\text{Te}_{2.01}$  nanowhiskers. (a) EDS spectrum of a  $T_d\text{-Mo}_{0.26}\text{W}_{0.73}\text{Te}_{2.01}$  nanowhisker (with its TEM image presented in the inset) shows the constituent elements of Mo, W, and Te. The Cu signals in the EDS spectrum are due to the Cu TEM grid. (b) EDS mappings (rightmost column) of the green demarcated region in the SEM image (left panel) show the uniform elemental distributions (Mo, W, and Te) along the CC fiber. (c) HR-TEM image displays the lattice spacings along the  $a$ - and  $b$ -axes, respectively. (d) SAED pattern along the  $\langle 001 \rangle$  direction shows an orthorhombic crystal. (e–h) The compositional analysis and crystal characterization of  $1T'$ - &  $T_d\text{-Mo}_{0.66}\text{W}_{0.32}\text{Te}_{2.02}$  nanowhiskers were conducted following the same procedures presented in panels (a–d) for  $T_d\text{-Mo}_{0.26}\text{W}_{0.73}\text{Te}_{2.01}$  nanowhiskers. (g) HR-TEM image of  $1T'$ - &  $T_d\text{-Mo}_{0.66}\text{W}_{0.32}\text{Te}_{2.02}$  nanowhiskers. The image of the region marked by a green dashed square is magnified in the inset to show the tilting  $b$ -axis, highlighted by the nonlinear red–blue dotted lines. (h) SAED pattern along the  $\langle 001 \rangle$  direction demonstrates the co-existence of the orthorhombic ( $T_d$ ) and monoclinic ( $1T'$ ) phases with a tilt angle of  $4^\circ$  between both phases.

$\text{Mo}_x\text{W}_{1-x}\text{Te}_2/\text{CC}$  nanowhiskers in a specific crystallographic orientation. The peak positions in the XRD spectra obtained in this work are similar to the powder diffraction file data of 01-071-2156 and 01-071-2157. Compared with the peak intensities of  $T_d\text{-Mo}_{0.26}\text{W}_{0.73}\text{Te}_2/\text{CC}$  in the XRD spectrum, an intensity drop was observed in  $1T'$  &  $T_d\text{-Mo}_{0.66}\text{W}_{0.32}\text{Te}_{2.02}$ , indicating the reduced crystallinity due to the mixed phases in the sample. The (002) signal of  $1T'$  &  $T_d\text{-Mo}_{0.66}\text{W}_{0.32}\text{Te}_{2.02}/\text{CC}$  shows a peak shift of  $0.05^\circ$  to the lower angle side and a peak broadening, relative to  $T_d\text{-Mo}_{0.26}\text{W}_{0.73}\text{Te}_{2.01}/\text{CC}$ , revealing different crystalline domain sizes of the two samples. The asymmetric line shape of (004) with a shoulder at the lower angle side is contributed from the carbon cloth.<sup>54</sup> The peak broadening due to the reduced domain size,  $D$ , has been calculated using the Scherrer's formula of  $D = K\lambda/\beta\cos\theta$  where  $K$  denotes the Scherrer's constant of 0.9 and  $\beta$  is the full width at half-maximum (FWHM, in radians) of the peak. The FWHMs of (002) are  $0.33^\circ$  for  $T_d\text{-Mo}_{0.26}\text{W}_{0.73}\text{Te}_{2.01}/\text{CC}$  and

$0.45^\circ$  for  $1T'$  &  $T_d\text{-Mo}_{0.66}\text{W}_{0.32}\text{Te}_{2.02}$ , corresponding to the calculated domain sizes of 21.6 and 15.9 nm, respectively. As compared to  $T_d\text{-Mo}_{0.26}\text{W}_{0.73}\text{Te}_{2.01}/\text{CC}$ , the reduced domain size in  $1T'$  &  $T_d\text{-Mo}_{0.66}\text{W}_{0.32}\text{Te}_{2.02}$  thus provides more grain boundaries, giving rise to more seeding locations for a higher density of whisker growth. Moreover, it has been studied<sup>55</sup> that the domain size affects the surface charge density wave (SCDW) dynamics where the smaller domains result in the larger SCDW amplitudes. As a representative example, the Peierls-type lattice distortion and the presence of SCDW in  $1T'$ - $\text{MoTe}_2$  were reported to enhance electrocatalytic activity.<sup>17</sup> In this study,  $1T'$  &  $T_d\text{-Mo}_{0.66}\text{W}_{0.32}\text{Te}_{2.02}/\text{CC}$  owns the higher composition ratio of  $\text{MoTe}_2$  in the alloy, a smaller domain size, and likely the more enhanced SCDW than  $T_d\text{-Mo}_{0.26}\text{W}_{0.73}\text{Te}_{2.01}/\text{CC}$ , consequently leading to the better electrocatalytic performance of  $1T'$  &  $T_d\text{-Mo}_{0.66}\text{W}_{0.32}\text{Te}_{2.02}/\text{CC}$ , as will be demonstrated in the following sections.

The elemental compositions of the as-grown  $\text{Mo}_x\text{W}_{1-x}\text{Te}_2/\text{CC}$  were determined by XPS. Shown in Figure 2b are the XPS spectra of  $\text{Mo}_x\text{W}_{1-x}\text{Te}_2$  nanowhiskers, including the doublets resulted from the spin-orbit couplings in Mo, W, and Te, respectively. The elemental compositions were determined quantitatively by integrating the peak intensities of Mo  $3d_{5/2}$ , W  $4f_{7/2}$ , and Te  $3d_{5/2}$  with individual atomic sensitive factors considered, i.e., 1.66 for Mo  $3d_{5/2}$ , 1.76 for W  $4f_{7/2}$ , and 5.71 for Te  $3d_{5/2}$ . The composition ratios of the synthesized nanowhiskers were determined to be  $\text{Mo}_{0.26}\text{W}_{0.73}\text{Te}_{2.01}$  and  $\text{Mo}_{0.66}\text{W}_{0.32}\text{Te}_{2.02}$  of which the crystal phases correspond to a pure  $T_d$  and a mixture of  $1T'$  &  $T_d$  phases, respectively, according to the previous studies.<sup>21,45</sup> The observed blue shift of  $\sim 0.3$  eV and spectral broadening in  $1T'$  &  $T_d$ - $\text{Mo}_{0.66}\text{W}_{0.32}\text{Te}_{2.02}/\text{CC}$ , as compared with  $T_d$ - $\text{Mo}_{0.26}\text{W}_{0.73}\text{Te}_{2.01}$ , support the co-existence of the  $T_d$  and  $1T'$  phases.<sup>21</sup> In addition, the XPS spectra of the as-grown  $\text{MoTe}_2$  and  $\text{WTe}_2$  nanowhiskers are also presented in Figure S3 of the Supporting Information.

The phase identification and alloy features of the as-synthesized  $\text{Mo}_x\text{W}_{1-x}\text{Te}_2$  nanowhiskers were further examined by Raman spectroscopy (Figure 2c). We identified the phonon modes of  $\text{MoTe}_2$  nanowhiskers at 83 ( $A_2^2$ ), 105 ( $A_1^3$ ), 126 ( $A_1^5$ ), 161 ( $A_1^7$ ), and 262  $\text{cm}^{-1}$  ( $A_1^{11}$ ) and those of  $\text{WTe}_2$  nanowhiskers at 82 ( $A_2^2$ ), 107 ( $A_1^3$ ), 131 ( $A_1^5$ ), 160 ( $A_1^7$ ), and 208  $\text{cm}^{-1}$  ( $A_1^9$ ) in which the spectral assignments are consistent with the literature reports.<sup>20,48</sup> Both  $T_d$ - $\text{Mo}_{0.26}\text{W}_{0.73}\text{Te}_{2.01}$  and  $1T'$  &  $T_d$ - $\text{Mo}_{0.66}\text{W}_{0.32}\text{Te}_{2.02}/\text{CC}$  have a similar vibrational pattern consisting of a strong  $A_1^7$  band and an intermediate  $A_1^9$  band with their intensities proportional to the composition ratios of Mo:W.<sup>42,45</sup>

To characterize the crystal structures, HR-TEM was used to investigate  $T_d$ - $\text{Mo}_{0.26}\text{W}_{0.73}\text{Te}_{2.01}$  (Figure 3a–d) and  $1T'$  &  $T_d$ - $\text{Mo}_{0.66}\text{W}_{0.32}\text{Te}_{2.02}/\text{CC}$  (Figure 3e–h). The elemental compositions of Mo, W, and Te in  $T_d$ - $\text{Mo}_{0.26}\text{W}_{0.73}\text{Te}_{2.01}$  were examined by EDS (Figure 3a), and the uniform distribution of constituent elements in the nanowhiskers decorated on CC fibers was demonstrated by EDS mapping (Figure 3b). The HR-TEM image shows the lattice constants of  $a = 0.62$  nm and  $b = 0.35$  nm for the orthorhombic  $T_d$  crystal (Figure 3c) in which the lattice spacings are further supported by the plot profiles along the  $a$ - and  $b$ -axes (Figure S4a of the Supporting Information). The structural uniformity and high crystallinity over a wide area are supported by the selected area electron diffraction (SAED) pattern along  $\langle 001 \rangle$  where the observed lattices in the  $90^\circ$  orientation ( $\beta$  value) once more support an orthorhombic crystal structure (Figure 3d). Similarly, the EDS spectrum and mappings also show the uniform elemental distributions of  $1T'$  &  $T_d$ - $\text{Mo}_{0.66}\text{W}_{0.32}\text{Te}_{2.02}$  nanowhiskers along the CC fibers (Figure 3e,f). The HR-TEM image in Figure 3g shows the co-existence of orthorhombic ( $T_d$ ) and monoclinic ( $1T'$ ) crystals in  $1T'$  &  $T_d$ - $\text{Mo}_{0.66}\text{W}_{0.32}\text{Te}_{2.02}$  nanowhiskers of which the structural analysis is consistent with our earlier results observed by XPS and Raman spectroscopy.

Although the HR-TEM image (Figure 3g) of  $1T'$  &  $T_d$ - $\text{Mo}_{0.66}\text{W}_{0.32}\text{Te}_{2.02}$  shows similar lattice constants to those of the  $T_d$  phase (see the lattice plot profiles in Figure S4b of the Supporting Information), the  $b$ -axis was found to tilt (with a magnified image represented in the inset of Figure 3g for the region demarcated by a green dotted square), suggesting the presence of an additional phase. This observation is consistent with the literature report that both  $T_d$  and  $1T'$  phases have similar lattice spacings but differ in the  $\beta$  values by  $\sim 4^\circ$ .<sup>56</sup> In

Figure 3h, the analysis for the SAED pattern of  $1T'$  &  $T_d$ - $\text{Mo}_{0.66}\text{W}_{0.32}\text{Te}_{2.02}$  nanowhiskers reveals that the  $T_d$  and  $1T'$  phases co-exist in the crystal with a tilt angle of  $\sim 4^\circ$ , giving a  $\beta$  value of  $\sim 94^\circ$ . The HR-TEM images and SAED patterns of both  $\text{MoTe}_2$  and  $\text{WTe}_2$  are also presented in Figure S5 of the Supporting Information.

To evaluate the electrocatalytic performance of the as-grown  $\text{Mo}_x\text{W}_{1-x}\text{Te}_2/\text{CC}$ s used as different CEs in a DSSC, we conducted the parameter measurements in a custom-made DSSC system. As illustrated in Figure 4a, the DSSC system

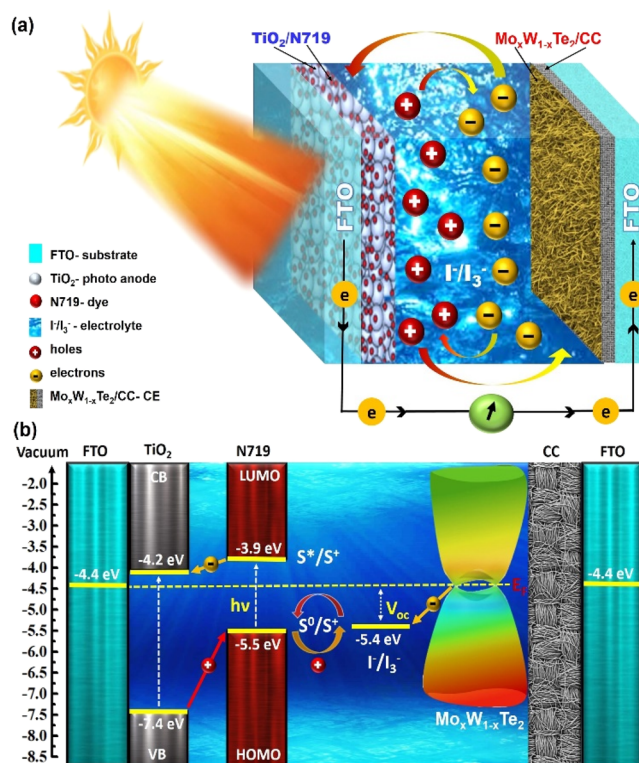


**Figure 4.** (a) An illustration represents the DSSC system used in this study, which consists of a TiO<sub>2</sub> nanoparticle-coated FTO photoanode decorated with N719 dye molecules and a Mo<sub>x</sub>W<sub>1-x</sub>Te<sub>2</sub>/CC CE for the reduction of I<sub>3</sub><sup>-</sup> ions. (b) An energy band diagram depicts the respective components in the DSSC system (S<sup>0</sup>: the ground electronic state (HOMO), S<sup>+</sup>: the hole left after photoexcitation, and S<sup>\*</sup>: the excited state (LUMO) of the dye molecule).

consists of a TiO<sub>2</sub> nanoparticle-coated fluorine-doped SnO<sub>2</sub> (FTO) photoanode decorated with N719 dye molecules and a Mo<sub>x</sub>W<sub>1-x</sub>Te<sub>2</sub>/CC CE to assist the electrocatalytic performance in the iodide/triiodide (denoted by I<sup>-</sup>/I<sub>3</sub><sup>-</sup>) redox reaction. Upon sunlight illumination, the N719 dye absorbs photons followed by injecting the excited electrons to the conduction band of the TiO<sub>2</sub> of a mesoporous network. Transported by the FTO substrate, the migrating electrons transfer to the Mo<sub>x</sub>W<sub>1-x</sub>Te<sub>2</sub>/CC-based CE through an external electrical load and subsequently pass over to the I<sup>-</sup>/I<sub>3</sub><sup>-</sup> electrolyte. At this stage, the oxidized N719 dye molecules, induced by the photoexcitation, are restored by the electron transfer from the electrolytic iodide/triiodide oxidation (i.e.,  $3\text{I}^- \rightarrow \text{I}_3^- + 2\text{e}^-$ ). The I<sup>-</sup> ions are further regenerated on the Mo<sub>x</sub>W<sub>1-x</sub>Te<sub>2</sub>/CC CE surface via the reduction reaction of  $\text{I}_3^- + 2\text{e}^- \rightarrow 3\text{I}^-$  to make the circuit completed. An energy band diagram to present this oxide/dye/electrolyte/electrocatalyst (i.e., TiO<sub>2</sub>/N719/I<sup>-</sup>/Mo<sub>x</sub>W<sub>1-x</sub>Te<sub>2</sub>/CC) system and the charge transfers

of electrons and holes involved in the whole system through these interfaces are illustrated in Figure 4b.

Within the DSSC system, a CE is used for the reduction of  $I_3^-$  ions, i.e.,  $I_3^- + 2e^- \rightarrow 3I^-$ ; the electrocatalytic ability of the CE is studied by cyclic voltammetry (CV) analysis. Herein, we investigated the electrocatalytic ability of five CEs, including Pt/CC,  $1T'$ - &  $T_d$ - $Mo_{0.66}W_{0.32}Te_{2.02}/CC$ ,  $T_d$ - $Mo_{0.26}W_{0.73}Te_{2.01}/CC$ ,  $MoTe_2/CC$ , and  $WTe_2/CC$  (represented as the five tested CEs hereafter). As shown in Figure 5a,

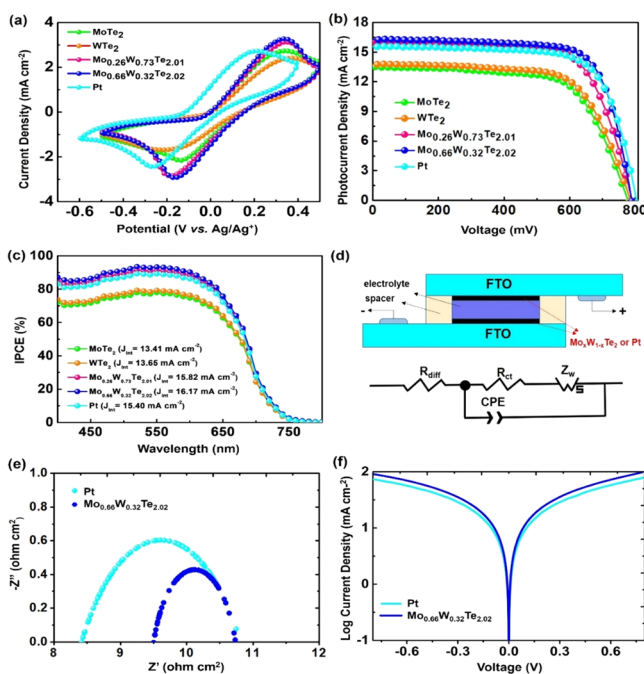


**Figure 5.** (a) The CV plots were measured for the five tested CEs to compare with the standard Pt/CC electrode. (b) The photocurrent density-voltage ( $J$ - $V$ ) curves with AM 1.5G illumination at  $100 \text{ mW cm}^{-2}$  and (c) their corresponding IPCE curves are measured. (d) A schematic illustration represents the symmetric cell employed in the EIS measurements. Comparisons of (e) EIS measurements and (f) Tafel analyses are made for a symmetric cell fabricated with  $1T'$ - &  $T_d$ - $Mo_{0.66}W_{0.32}Te_{2.02}/CC$  or Pt/CC on both the anode and cathode.

the higher cathodic peak current density ( $J_{PC}$ ) reflects the better electrocatalytic activity for the reduction of  $I_3^-$  ions. The  $J_{PC}$  values of the five tested CEs follow the order of  $1T'$ - &  $T_d$ - $Mo_{0.66}W_{0.32}Te_{2.02}/CC$  ( $-2.73 \text{ mA cm}^{-2}$ ) >  $T_d$ - $Mo_{0.26}W_{0.73}Te_{2.01}/CC$  ( $-2.66 \text{ mA cm}^{-2}$ ) > Pt/CC ( $-2.03 \text{ mA cm}^{-2}$ ) >  $MoTe_2/CC$  ( $-1.87 \text{ mA cm}^{-2}$ ) >  $WTe_2/CC$  ( $-1.32 \text{ mA cm}^{-2}$ ). The separation ( $\Delta E_p$ ) between the oxidation and reduction peaks shows an order of  $T_d$ - $Mo_{0.26}W_{0.73}Te_{2.01}/CC$  (0.50 V) >  $WTe_2/CC$  (0.47 V) >  $1T'$ - &  $T_d$ - $Mo_{0.66}W_{0.32}Te_{2.02}/CC$  (0.46 V) >  $MoTe_2/CC$  (0.42 V)  $\approx$  Pt/CC (0.42 V). We found that the  $\Delta E_p$  value of the Mo-rich sample is closer to that of the Pt/CC sample; however, the mechanism for this outcome needs further investigation. A comparative electrocatalytic performance of Pt on an FTO substrate is also shown in Figure S6 and Table S1 of the Supporting Information.

The poor electrocatalytic activities of the binary compounds of  $Mo_xW_{1-x}Te_2/CC$  (i.e.,  $x = 1$  for  $MoTe_2/CC$  and  $x = 0$  for  $WTe_2/CC$ ), as compared with the ternary compounds of  $T_d$ - $Mo_{0.26}W_{0.73}Te_{2.01}/CC$  and  $1T'$ - &  $T_d$ - $Mo_{0.66}W_{0.32}Te_{2.02}/CC$ , can be explained by the following reasons. As mentioned

earlier, the easy phase transition from  $1T'$  to  $2H$  occurs at  $Mo_xW_{1-x}Te_2$  ( $x \geq 0.96$ ), making  $MoTe_2$  a semiconductor rather than a semi-metal. On the other hand,  $WTe_2$  is subject to oxidation under an ambient condition, consequently deteriorating its electrocatalytic ability. In contrast, the ternary compounds of WSM  $Mo_xW_{1-x}Te_2$  alloys are highly stable against phase transition and surface oxidation. Compared with a Pt/CC, the larger  $J_{PC}$  of the ternary  $Mo_xW_{1-x}Te_2$  CEs could be due to the larger surface areas contributed from the vertically aligned WSM  $Mo_xW_{1-x}Te_2$  nanowhiskers on CC fibers. These  $Mo_xW_{1-x}Te_2/CC$  CEs with large surface areas and semi-metallic nature become an effective candidate to replace Pt in electrocatalysis. Furthermore,  $1T'$ - &  $T_d$ - $Mo_{0.66}W_{0.32}Te_{2.02}/CC$  shows a slightly higher  $J_{PC}$  than that of the  $T_d$ - $Mo_{0.26}W_{0.73}Te_{2.01}/CC$ . Accordingly, the superior cell efficiency of a  $1T'$ - &  $T_d$ - $Mo_{0.66}W_{0.32}Te_{2.02}/CC$  CE in DSSCs can be expected.

Next, the photovoltaic performance of the five tested CEs was investigated with their photocurrent density versus voltage ( $J$ - $V$ ) curves shown in Figure 5b. The photovoltaic parameter analysis for the photocurrent density ( $J_{SC}$ ) indicates that  $1T'$ - &  $T_d$ - $Mo_{0.66}W_{0.32}Te_{2.02}/CC$  ( $16.29 \text{ mA cm}^{-2}$ ) is higher than  $T_d$ - $Mo_{0.26}W_{0.73}Te_{2.01}/CC$  ( $16.01 \text{ mA cm}^{-2}$ ) and Pt/CC ( $15.57 \text{ mA cm}^{-2}$ ). Meanwhile,  $MoTe_2$  and  $WTe_2$  exhibit much lower  $J_{SC}$  values of  $13.54$  and  $13.78 \text{ mA cm}^{-2}$ , respectively. The higher  $J_{SC}$  values of  $Mo_xW_{1-x}Te_2/CC$  are again ascribed to the vertically aligned nanowhiskers on CC fibers to gain more surface areas for electrocatalysis, as compared with the constrained electrocatalytic surface area of the sputtered Pt layer. In the DSSC test, the  $MoTe_2/CC$ - and  $WTe_2/CC$ -based CEs show relatively low efficiencies ( $\eta$ ) of 6.97 and 7.27%, respectively. In contrast to the  $\eta = 8.79\%$  of  $T_d$ - $Mo_{0.26}W_{0.73}Te_{2.01}/CC$  CE, the  $\eta$  of  $1T'$ - &  $T_d$ - $Mo_{0.66}W_{0.32}Te_{2.02}/CC$  CE reaches 9.40%, which is  $\sim 5\%$  higher than that (8.93%) of a standard Pt/CC CE. The electrocatalytic efficiencies of  $Mo_xW_{1-x}Te_2$  nanowhiskers with different stoichiometric ratios decorated on CC fibers are compared in Figure S7 of the Supporting Information. The best  $\eta$  of a  $1T'$ - &  $T_d$ - $Mo_{0.66}W_{0.32}Te_{2.02}/CC$  CE stems from the fact that the vertically-aligned  $1T'$ - &  $T_d$ - $Mo_{0.66}W_{0.32}Te_{2.02}$  nanowhiskers on CC fibers provide not only large electrocatalytic areas but also efficient charge transfers via nanowhiskers for the reduction of  $I_3^- + 2e^- \rightarrow 3I^-$ . Furthermore, the semi-metallic  $1T'$ - &  $T_d$ - $Mo_{0.66}W_{0.32}Te_{2.02}$  nanowhiskers hold high charge mobility and demonstrate robust WSM surface states to boost the charge transport from the CE surface to the redox ions in a DSSC, thereby enhancing the reaction kinetics and acting as the best CE among the five tested samples. For the power conversion efficiency in a DSSC, the  $1T'$ - &  $T_d$ - $Mo_{0.66}W_{0.32}Te_{2.02}/CC$  CE is superior to the recently reported thin films or heterostructures of a  $MoTe_2$ -based CE.<sup>40,57</sup> Notwithstanding the reported efficiencies of the  $CoSe_2$  coated on CC (or a nickel foam) to own  $\eta = 9.87\%$  (or 10.46%),<sup>27</sup> the electrocatalytic efficiency of  $Mo_xW_{1-x}Te_2$  nanowhiskers can be further enhanced by decorating on various supporting substrates, e.g., graphene hybrids, polymer composites, etc.

In Figure 5c, the incident photon-to-electron conversion efficiency (IPCE) of a DSSC comprising one of the five tested CEs was measured. The calculated photocurrent densities ( $J_{IPCE}$ ) are summarized in Figure 5c by integrating IPCE with the AM 1.5G solar light spectrum. In the DSSC applications, it is noted that the increasing order of the  $J_{IPCE}$  values,  $MoTe_2/CC$  ( $13.41 \text{ mA cm}^{-2}$ ) <  $WTe_2/CC$  ( $13.65 \text{ mA cm}^{-2}$ ) < Pt/CC

(15.40 mA cm<sup>-2</sup>) <  $T_d$ -Mo<sub>0.26</sub>W<sub>0.73</sub>Te<sub>2.01</sub>/CC (15.82 mA cm<sup>-2</sup>) <  $1T'$ - &  $T_d$ -Mo<sub>0.66</sub>W<sub>0.32</sub>Te<sub>2.02</sub>/CC (16.17 mA cm<sup>-2</sup>), agrees with the above  $J_{SC}$  values in the  $J$ - $V$  curves shown in Figure 5b and Table 1. Moreover, the photovoltaic perform-

**Table 1. The Photovoltaic Parameters of a DSSC with Different CEs Were Measured under AM 1.5G Illumination at 100 mW Cm<sup>-2</sup>**

counter electrodes	$\eta$ (%)	$V_{oc}$ (mV)	$J_{sc}$ (mA cm <sup>-2</sup> )	FF
MoTe <sub>2</sub> /CC	6.97	778	13.54	0.66
WTe <sub>2</sub> /CC	7.27	784	13.78	0.67
Mo <sub>0.26</sub> W <sub>0.73</sub> Te <sub>2.01</sub> /CC	8.79	790	16.01	0.70
Mo <sub>0.66</sub> W <sub>0.32</sub> Te <sub>2.02</sub> /CC	9.40	788	16.29	0.73
Pt/CC	8.93	804	15.57	0.71

ance of  $1T'$ - &  $T_d$ -Mo<sub>0.66</sub>W<sub>0.32</sub>Te<sub>2.02</sub> nanowhiskers-fabricated CEs in a DSSC is reproducible as tested in Figure S8 and Table S2 of the Supporting Information.

The interfacial charge-transfer kinetics on the CEs of a DSSC was investigated by electrochemical impedance spectroscopy (EIS). Figure 5d shows a symmetric dummy cell with its equivalent circuit model to analyze the measured EIS data.<sup>58–60</sup> In this test, we compared the best selected  $1T'$  &  $T_d$ -Mo<sub>0.66</sub>W<sub>0.32</sub>Te<sub>2.02</sub>/CC with a standard Pt/CC using a symmetric cell where both the anode and cathode were made with the same electrocatalyst. The FRA2 module was controlled with an AC amplitude of  $\pm 10$  mV in an open-circuit condition at a frequency between 10 mHz and 100 kHz. Generally, the EIS spectrum of a symmetrical dummy cell should exhibit two semicircles within the frequency range of measurements. The first semicircle represents the charge-transfer resistance at the interface of electrode/electrolyte ( $R_{ct}$ ), and the second semicircle refers to the Warburg diffusion process of  $\Gamma/I_3^-$  ions in the electrolyte ( $R_{diff}$ ). However, in this work, only one semicircle was observed. Here, the second semicircle could have merged with the first semicircle due to the low viscosity (i.e., high ion diffusivity) of the electrolyte used. From Figure 5e, it is clear that the  $R_{ct}$  values of the electrocatalytic electrodes reveal  $1T'$ - &  $T_d$ -Mo<sub>0.66</sub>W<sub>0.32</sub>Te<sub>2.02</sub>/CC < Pt/CC (see  $R_{ct-EIS}$  in Table 2). The lower  $R_{ct}$  value of a

**Table 2. DSSC Parameters Extracted from the EIS and Tafel Plots Shown in Figure 5e,f**

counter electrodes	$J_0$ (mA cm <sup>-2</sup> )	$R_{ct-Tafel}$ (ohm cm <sup>2</sup> )	$R_{ct-EIS}$ (ohm cm <sup>2</sup> )
Pt/CC	9.51	1.35	1.19
Mo <sub>0.66</sub> W <sub>0.32</sub> Te <sub>2.02</sub> /CC	12.47	1.03	0.62

symmetric cell is attributed to the minimal loss of internal energy at the electrode/electrolyte interface, indicating the high efficacy in the reduction reaction of  $I_3^- + 2e^- \rightarrow 3I^-$  at the electrocatalytic electrode. Consequently, the lower  $R_{ct}$  of  $1T'$  &  $T_d$ -Mo<sub>0.66</sub>W<sub>0.32</sub>Te<sub>2.02</sub>/CC yielded a more efficient DSSC. Meanwhile, the Tafel polarization curve (Figure 5f) was also applied to examine the charge-transfer resistance in the above mentioned symmetric cells. The exchange current density ( $J_0$ ) was obtained from the logarithmic current density ( $\log J$ ) plotted as a function of the voltage ( $V$ ) of electrocatalytic electrode (Figure 5f). The  $J_0$  value is the  $y$ -axis intercept obtained by extrapolating the anodic or cathodic curves in the Tafel zone ( $120 \text{ mV} < |V| < 400 \text{ mV}$ ). The equation of  $R \times T / (n \times F \times J_0)$  was used to determine the charge-transfer

resistance ( $R_{ct-Tafel}$ ) of an electrode at the electrode/electrolyte interface where  $R$  is the ideal gas constant and  $T$  is the absolute temperature. The decrease in  $R_{ct-Tafel}$  and increase in  $J_0$  enhanced the electrocatalytic activity of the electrode. The  $J_0$  values in Table 2 show a trend of  $1T'$  &  $T_d$ -Mo<sub>0.66</sub>W<sub>0.32</sub>Te<sub>2.02</sub>/CC > Pt/CC, demonstrating the excellent charge-transfer characteristics (i.e., the low  $R_{ct-Tafel}$ ) of the  $1T'$  &  $T_d$ -Mo<sub>0.66</sub>W<sub>0.32</sub>Te<sub>2.01</sub>/CC electrode.

Ultimately, we examined the long-term stabilities of the CEs made of  $1T'$ - &  $T_d$ -Mo<sub>0.66</sub>W<sub>0.32</sub>Te<sub>2.02</sub>/CC and Pt/CC, respectively, by continuously scanning the CV measurements for 100 cycles in the  $\Gamma/I_3^-$  redox reaction (Figure S9a,b of the Supporting Information). Normally, a stable electrocatalytic electrode should have no change in the maximum current density as the number of scanning cycles increases. In Figure S9a, while the  $J_{PC}$  values of  $1T'$ - &  $T_d$ -Mo<sub>0.66</sub>W<sub>0.32</sub>Te<sub>2.02</sub>/CC sustained for 100-cycle CV scans, those of Pt/CC (Figure S9b) decrease, probably suffering from the surface contamination and/or Pt-dissolution in the  $\Gamma/I_3^-$  electrolyte as mentioned in previous reports.<sup>61</sup> The long-term stability at rest of the DSSC using a  $1T'$  &  $T_d$ -Mo<sub>0.66</sub>W<sub>0.32</sub>Te<sub>2.02</sub>/CC was also examined as shown in Figure S10 of the Supporting Information in which the corresponding photovoltaic parameters remained almost constant without falling during the test period of 15 days. This result validates that the topologically protected WSM surface of a  $1T'$ - &  $T_d$ -Mo<sub>0.66</sub>W<sub>0.32</sub>Te<sub>2.02</sub>-based CE holds superior electrocatalytic durability over 100 redox cycles in the  $\Gamma/I_3^-$  electrolyte. Also, from the photovoltaic parameter analysis, the minimal charge-transfer resistance of a  $1T'$  &  $T_d$ -Mo<sub>0.66</sub>W<sub>0.32</sub>Te<sub>2.02</sub>/CC CE could enhance catalytic activity, which makes the  $1T'$  &  $T_d$ -Mo<sub>0.66</sub>W<sub>0.32</sub>Te<sub>2.02</sub>/CC CE superior to other TMD-based CEs under the similar test conditions in a DSSC (Section S9 and Table S3 of the Supporting Information).

## CONCLUSIONS

In this work, we synthesized stoichiometry-controlled nanowhiskers of  $1T'$ -MoTe<sub>2</sub>,  $T_d$ -Mo<sub>0.26</sub>W<sub>0.73</sub>Te<sub>2.01</sub>,  $1T'$ - &  $T_d$ -Mo<sub>0.66</sub>W<sub>0.32</sub>Te<sub>2.02</sub>, and  $T_d$ -WTe<sub>2</sub> on CC substrates, which were then employed as CEs in a DSSC for testing their electrochemical activities and efficiencies. The CV measurements in the  $\Gamma/I_3^-$  electrolyte over 100 cycles demonstrated that Mo<sub>*x*</sub>W<sub>1-*x*</sub>Te<sub>2</sub>/CC is more stable than Pt/CC. In the DSSC performance tests,  $1T'$ - &  $T_d$ -Mo<sub>0.66</sub>W<sub>0.32</sub>Te<sub>2.02</sub>/CC can reach a photocurrent density of 16.29 mA cm<sup>-2</sup>, a maximum IPCE of 90% at 550 nm excitation, and an efficiency of  $\eta = 9.40\%$ , the efficiency of which is better than Pt/CC (8.93%),  $T_d$ -Mo<sub>0.26</sub>W<sub>0.73</sub>Te<sub>2.01</sub>/CC (8.79%),  $T_d$ -WTe<sub>2</sub>/CC (7.27%), and  $1T'$ -MoTe<sub>2</sub>/CC (6.97%). From the EIS analyses,  $1T'$ - &  $T_d$ -Mo<sub>0.66</sub>W<sub>0.32</sub>Te<sub>2.02</sub>/CC exhibits lower charge-transfer resistance (0.62  $\Omega$  cm<sup>2</sup>) than a Pt/CC (1.19  $\Omega$  cm<sup>2</sup>) in electrocatalytic reactions.  $1T'$  &  $T_d$ -Mo<sub>0.66</sub>W<sub>0.32</sub>Te<sub>2.02</sub>/CC nanowhiskers of smaller crystalline domain sizes could enhance SCDW for better electrocatalytic performance. Moreover, a  $1T'$  &  $T_d$ -Mo<sub>0.66</sub>W<sub>0.32</sub>Te<sub>2.02</sub>/CC-based CE of minimal charge-transfer resistance is beneficial for the reaction kinetics in DSSCs. The experimental results of this work demonstrate that topologically protected WSM  $1T'$ - &  $T_d$ -Mo<sub>0.66</sub>W<sub>0.32</sub>Te<sub>2.02</sub> nanowhiskers with high electrical mobility and robust surface states are a favorable alternative to replace Pt in the electrocatalytic applications.

## ■ ASSOCIATED CONTENT

### SI Supporting Information

The Supporting Information is available free of charge at <https://pubs.acs.org/doi/10.1021/acsami.0c07075>.

(S1) Growth of  $\text{Mo}_x\text{W}_{1-x}\text{Te}_2$  nanowiskers in APCVD reactions, (S2) scanning electron microscopy (SEM), (S3) X-ray photoelectron spectroscopy (XPS), (S4) high-resolution transmission electron microscopy (HR-TEM), (S5) electrochemical experiments, (S6) comparison of electrocatalytic performance, (S7) reproducibility test, (S8) long-term stability tests, and (S9) comparison of photovoltaic parameters (PDF)

## ■ AUTHOR INFORMATION

### Corresponding Author

**Yit-Tsong Chen** – Institute of Atomic and Molecular Sciences, Academia Sinica, Taipei 10617, Taiwan; Department of Chemistry, National Taiwan University, Taipei 10617, Taiwan; [orcid.org/0000-0002-6204-8320](https://orcid.org/0000-0002-6204-8320); Email: [ytchem@ntu.edu.tw](mailto:ytchem@ntu.edu.tw)

### Authors

**Roshan Jesus Mathew** – Department of Engineering and System Science, National Tsing-Hua University, Hsinchu 30013, Taiwan; Nano-Science and Technology Program, Taiwan International Graduate Program and Institute of Atomic and Molecular Sciences, Academia Sinica, Taipei 11529, Taiwan; [orcid.org/0000-0002-0913-6321](https://orcid.org/0000-0002-0913-6321)

**Chuan-Pei Lee** – Department of Applied Physics and Chemistry, University of Taipei, Taipei 10048, Taiwan

**Chi-Ang Tseng** – Department of Chemistry, National Taiwan University, Taipei 10617, Taiwan

**Pradyumna Kumar Chand** – Department of Chemistry, National Taiwan University, Taipei 10617, Taiwan

**Yi-June Huang** – Department of Chemical Engineering, National Taiwan University, Taipei 10617, Taiwan

**Han-Ting Chen** – Department of Chemical Engineering, National Taiwan University, Taipei 10617, Taiwan; [orcid.org/0000-0002-6942-718X](https://orcid.org/0000-0002-6942-718X)

**Kuo-Chuan Ho** – Department of Chemical Engineering, National Taiwan University, Taipei 10617, Taiwan; [orcid.org/0000-0001-7501-1271](https://orcid.org/0000-0001-7501-1271)

**Aswin kumar Anbalagan** – Department of Engineering and System Science, National Tsing-Hua University, Hsinchu 30013, Taiwan; [orcid.org/0000-0001-5511-2083](https://orcid.org/0000-0001-5511-2083)

**Chih-Hao Lee** – Department of Engineering and System Science, National Tsing-Hua University, Hsinchu 30013, Taiwan; [orcid.org/0000-0002-3898-6421](https://orcid.org/0000-0002-3898-6421)

Complete contact information is available at: <https://pubs.acs.org/doi/10.1021/acsami.0c07075>

### Author Contributions

□ R.J.M. and C.-P.L. contributed equally to this work.

### Author Contributions

The manuscript was written through the contributions of all authors. All authors have approved the final version of the manuscript.

### Funding

This work was partly funded by the Ministry of Science and Technology of Taiwan under MOST 106-2113-M-002-022-MY3 and 107-2113-M-002-011-MY3.

## Notes

The authors declare no competing financial interest.

## ■ ACKNOWLEDGMENTS

R.J.M. is thankful for the support of the Taiwan International Graduate Program (TIGP) of Academia Sinica. Thanks to NSRRC for the allocation of beam time for this study. We acknowledge Mr. Han-Bang Chen of Instrumentation Center, National Taiwan University, for his assistance in XPS measurements and Ms. Chia-Ying Chien of Instrumentation Center, National Taiwan University, for her assistance in HR-TEM measurements.

## ■ REFERENCES

- (1) Hagfeldt, A.; Boschloo, G.; Sun, L.; Kloo, L.; Pettersson, H. Dye-Sensitized Solar Cells. *Chem. Rev.* **2010**, *110*, 6595–6663.
- (2) Yun, S.; Qin, Y.; Uhl, A. R.; Vlachopoulos, N.; Yin, M.; Li, D.; Han, X.; Hagfeldt, A. New-generation Integrated Devices Based on Dye-Sensitized and Perovskite Solar Cells. *Energy Environ. Sci.* **2018**, *11*, 476–526.
- (3) Cao, B.; Liu, H.; Yang, L.; Li, X.; Liu, H.; Dong, P.; Mai, X.; Hou, C.; Wang, N.; Zhang, J.; Fan, J.; Gao, Q.; Guo, Z. Interfacial Engineering for High-Efficiency Nanorod Array-Structured Perovskite Solar Cells. *ACS Appl. Mater. Interfaces* **2019**, *11*, 33770–33780.
- (4) Chen, H.; Luo, Q.; Liu, T.; Tai, M.; Lin, J.; Murugadoss, V.; Lin, H.; Wang, J.; Guo, Z.; Wang, N. Boosting Multiple Interfaces by Co-Doped Graphene Quantum Dots for High Efficiency and Durability Perovskite Solar Cells. *ACS Appl. Mater. Interfaces* **2020**, *12*, 13941–13949.
- (5) Ren, J.; Luo, Q.; Hou, Q.; Chen, H.; Liu, T.; He, H.; Wang, J.; Shao, Q.; Dong, M.; Wu, S.; Wang, N.; Lin, J.; Guo, Z. Suppressing Charge Recombination and Ultraviolet Light Degradation of Perovskite Solar Cells Using Silicon Oxide Passivation. *ChemElectroChem* **2019**, *6*, 3167.
- (6) Luo, Q.; Ma, H.; Hou, Q.; Li, Y.; Ren, J.; Dai, X.; Yao, Z.; Zhou, Y.; Xiang, L.; Du, H.; He, H.; Wang, N.; Jiang, K.; Lin, H.; Zhang, H.; Guo, Z. All-Carbon-Electrode-Based Endurable Flexible Perovskite Solar Cells. *Adv. Funct. Mater.* **2018**, *28*, 1706777.
- (7) Elayappan, V.; Murugadoss, V.; Fei, Z.; Dyson, P. J.; Angaiah, S. Influence of Polypyrrole Incorporated Electrospun Poly(vinylidene fluoride-co-hexafluoropropylene) Nanofibrous Composite Membrane Electrolyte on the Photovoltaic Performance of Dye Sensitized Solar Cell. *Engineered Sci.* **2020**, *78*.
- (8) Sharma, K.; Sharma, V.; Sharma, S. S. Dye-Sensitized Solar Cells: Fundamentals and Current Status. *Nanoscale Res. Lett.* **2018**, *13*, 381.
- (9) Waghmare, M. A.; Beedri, N. I.; Ubale, A. U.; Pathan, H. M. Fabrication and Characterization of Rose Bengal Sensitized Binary  $\text{TiO}_2$ - $\text{ZrO}_2$  Oxides Photo-electrode Based Dye-sensitized Solar Cell. *Engineered Sci.* **2019**, *6*, 36–43.
- (10) Murugadoss, V.; Panneerselvam, P.; Yan, C.; Guo, Z.; Angaiah, S. A Simple One-Step Hydrothermal Synthesis of Cobalt-nickel Selenide/Graphene Nanohybrid as an Advanced Platinum Free Counter Electrode for Dye Sensitized Solar Cell. *Electrochim. Acta* **2019**, *312*, 157–167.
- (11) Murugadoss, V.; Lin, J.; Liu, H.; Mai, X.; Ding, T.; Guo, Z.; Angaiah, S. Optimizing Graphene Content in a NiSe/Graphene Nanohybrid Counter Electrode to Enhance the Photovoltaic Performance of Dye-Sensitized Solar Cells. *Nanoscale* **2019**, *11*, 17579–17589.
- (12) Xu, T.; Kong, D.; Xi, Z.; Huang, T.; Qin, X.; Wu, H.; Kou, K.; Wang, R.; Chen, L.; Ma, T. Photoinduced Polyacrylate Based Polymer Electrolyte for Quasi-solid State Dye Sensitized Solar Cell Application. *Engineered Sci.* **2019**, *7*, 17–25.
- (13) Hecht, D. S.; Hu, L.; Irvin, G. Emerging Transparent Electrodes Based on Thin Films of Carbon Nanotubes, Graphene, and Metallic Nanostructures. *Adv. Mater.* **2011**, *23*, 1482–1513.

- (14) Qin, Q.; Zhang, R. A Novel Conical Structure of Polyaniline Nanotubes Synthesized on ITO-PET Conducting Substrate by Electrochemical Method. *Electrochim. Acta* **2013**, *89*, 726–731.
- (15) Balasingam, S. K.; Kang, M. G.; Jun, Y. Metal Substrate Based Electrodes for Flexible Dye-Sensitized Solar Cells: Fabrication Methods, Progress and Challenges. *Chem. Commun.* **2013**, *49*, 11457–11475.
- (16) O'Regan, B.; Grätzel, M. A Low-Cost, High-Efficiency Solar Cell Based on Dye-Sensitized Colloidal TiO<sub>2</sub> Films. *Nature* **1991**, *353*, 737–740.
- (17) Lv, Y.; Zhu, L.; Xu, H.; Yang, L.; Liu, Z.; Cheng, D.; Cao, X.; Yun, J.; Cao, D. Core/shell Template-derived Co, N-doped Carbon Bifunctional Electrocatalysts for Rechargeable Zn-air Battery. *Engineered Sci.* **2019**, *7*, 26–37.
- (18) Pan, D.; Ge, S.; Zhao, J.; Tian, J.; Shao, Q.; Guo, L.; Mai, X.; Wu, T.; Murugadoss, V.; Liu, H.; Ding, T.; Angaiah, S.; Guo, Z. Synthesis and Characterization of ZnNiIn Layered Double Hydroxides Derived Mixed Metal Oxides with Highly Efficient Photoelectrocatalytic Activities. *Ind. Eng. Chem. Res.* **2018**, *58*, 836–848.
- (19) Zhai, Y.; Wang, J.; Gao, Q.; Fan, Y.; Hou, C.; Hou, Y.; Liu, H.; Shao, Q.; Wu, S.; Zhao, L.; Ding, T.; Dang, F.; Guo, Z. Highly Efficient Cobalt Nanoparticles Anchored Porous N-Doped Carbon Nanosheets Electrocatalysts for Li-O<sub>2</sub> Batteries. *J. Catal.* **2019**, *377*, 534–542.
- (20) Yang, P.; Zhao, H.; Yang, Y.; Zhao, P.; Zhao, X.; Yang, L. Fabrication of N, P-codoped Mo<sub>2</sub>C/Carbon Nanofibers via Electrospinning as Electrocatalyst for Hydrogen Evolution Reaction. *ES Mater. Manuf.* **2020**, *7*, 34–39.
- (21) Wang, C.; Lan, F.; He, Z.; Xie, X.; Zhao, Y.; Hou, H.; Guo, L.; Murugadoss, V.; Liu, H.; Shao, Q.; Gao, Q.; Ding, T.; Wei, R.; Guo, Z. Iridium-Based Catalysts for Solid Polymer Electrolyte Electrocatalytic Water Splitting. *ChemSusChem* **2019**, *12*, 1576.
- (22) Abe, H.; Liu, J.; Ariga, K. Catalytic Nanoarchitectonics for Environmentally Compatible Energy Generation. *Mater. Today* **2016**, *19*, 12–18.
- (23) Manikandan, M.; Tanabe, T.; Ramesh, G. V.; Kodyath, R.; Ueda, S.; Sakuma, Y.; Homma, Y.; Dakshanamoorthy, A.; Ariga, K.; Abe, H. Tailoring the Surface-Oxygen Defects of a Tin Dioxide Support Towards an Enhanced Electrocatalytic Performance of Platinum Nanoparticles. *Phys. Chem. Chem. Phys.* **2016**, *18*, 5932–5937.
- (24) Low, T.; Chaves, A.; Caldwell, J. D.; Kumar, A.; Fang, N. X.; Avouris, P.; Heinz, T. F.; Guinea, F.; Martin-Moreno, L.; Koppens, F. Polaritons in Layered Two-Dimensional Materials. *Nat. Mater.* **2017**, *16*, 182–194.
- (25) Chen, T.-Y.; Liu, Y.-T.; Nguyen, H. M.; Fan, L.-J.; Wu, C.-Y.; Mark Luo, T.-J.; Lee, C.-H.; Yang, Y.-W.; Wen, T.-C.; Lin, T.-L. Ruthenium Core-Activated Platinum Monolayer Shell High Redox Activity Cathodic Electrocatalysts for Dye-Sensitized Solar Cells. *J. Mater. Chem. A* **2013**, *1*, 5660–5669.
- (26) Li, B. L.; Setyawati, M. I.; Chen, L.; Xie, J.; Ariga, K.; Lim, C.-T.; Garaj, S.; Leong, D. T. Directing Assembly and Disassembly of 2D MoS<sub>2</sub> Nanosheets with DNA for Drug Delivery. *ACS Appl. Mater. Interfaces* **2017**, *9*, 15286–15296.
- (27) Geim, A. K.; Grigorieva, I. V. Van der Waals Heterostructures. *Nature* **2013**, *499*, 419–425.
- (28) Singh, E.; Kim, K. S.; Yeom, G. Y.; Nalwa, H. S. Two-Dimensional Transition Metal Dichalcogenide-Based Counter Electrodes for Dye-Sensitized Solar Cells. *RSC Adv* **2017**, *7*, 28234–28290.
- (29) Ambrosi, A.; Sofer, Z.; Pumera, M. 2H → 1T Phase Transition and Hydrogen Evolution Activity of MoS<sub>2</sub>, MoSe<sub>2</sub>, WS<sub>2</sub> and WSe<sub>2</sub> Strongly Depends on the MX<sub>2</sub> Composition. *Chem. Commun.* **2015**, *51*, 8450–8453.
- (30) Rajamathi, C. R.; Gupta, U.; Kumar, N.; Yang, H.; Sun, Y.; Süß, V.; Shekhar, C.; Schmidt, M.; Blumtritt, H.; Werner, P.; Yan, B.; Parkin, S.; Felser, C.; Rao, C. N. R. Weyl Semimetals as Hydrogen Evolution Catalysts. *Adv. Mater.* **2017**, *29*, 1606202.
- (31) Liang, T.; Gibson, Q.; Ali, M. N.; Liu, M.; Cava, R. J.; Ong, N. P. Ultrahigh Mobility and Giant Magnetoresistance in the Dirac Semimetal Cd<sub>3</sub>As<sub>2</sub>. *Nat. Mater.* **2015**, *14*, 280–284.
- (32) Shekhar, C.; Nayak, A. K.; Sun, Y.; Schmidt, M.; Nicklas, M.; Leermakers, I.; Zeitler, U.; Skourski, Y.; Wosnitza, J.; Liu, Z.; Chen, Y.; Schnelle, W.; Borrmann, H.; Grin, Y.; Felser, C.; Yan, B. Extremely Large Magnetoresistance and Ultrahigh Mobility in the Topological Weyl Semimetal Candidate NbP. *Nat. Phys.* **2015**, *11*, 645–649.
- (33) Hosur, P.; Qi, X. Recent Developments in Transport Phenomena in Weyl Semimetals. *C. R. Phys.* **2013**, *14*, 857–870.
- (34) Politano, A.; Chiarello, G.; Li, Z.; Fabio, V.; Wang, L.; Guo, L.; Chen, X.; Boukhvalov, D. W. Toward the Effective Exploitation of Topological Phases of Matter in Catalysis: Chemical Reactions at the Surfaces of NbAs and TaAs Weyl Semimetals. *Adv. Funct. Mater.* **2018**, *28*, 1800511.
- (35) Wan, X.; Turner, A. M.; Vishwanath, A.; Savrasov, S. Y. Topological Semimetal and Fermi-Arc Surface States in the Electronic Structure of Pyrochlore Iridates. *Phys. Rev. B* **2011**, *83*, 205101.
- (36) Hasan, M. Z.; Kane, C. L. Colloquium: Topological Insulators. *Rev. Mod. Phys.* **2010**, *82*, 3045–3067.
- (37) Seok, J.; Lee, J. H.; Cho, S.; Ji, B.; Kim, H. W.; Kwon, M.; Kim, D.; Kim, Y. M.; Oh, S. H.; Kim, S. W.; Lee, Y. H.; Son, Y. W.; Yang, H. Active Hydrogen Evolution through Lattice Distortion in Metallic MoTe<sub>2</sub>. *2D Mater.* **2017**, *4*, No. 025061.
- (38) Luxa, J.; Vosecký, P.; Mazánek, V.; Sedmidubský, D.; Pumera, M.; Lazar, P.; Sofer, Z. Layered Transition Metal Ditellurides in Electrocatalytic Applications – Contrasting Properties. *ACS Catal.* **2017**, *7*, 5706.
- (39) Li, J.; Hong, M.; Sun, L.; Zhang, W.; Shu, H.; Chang, H. Enhanced Electrocatalytic Hydrogen Evolution from Large-Scale, Facile-Prepared, Highly Crystalline WTe<sub>2</sub> Nanoribbons with Weyl Semimetallic Phase. *ACS Appl. Mater. Interfaces* **2018**, *10*, 458.
- (40) Hussain, S.; Patil, S. A.; Vikraman, D.; Mengal, N.; Liu, H.; Song, W.; An, K.-S.; Jeong, S. H.; Kim, H.-S.; Jung, J. Large Area Growth of MoTe<sub>2</sub> Films as High Performance Counter Electrodes for Dye-Sensitized Solar Cells. *Sci. Rep.* **2018**, *8*, 29. 1
- (41) Chang, T.-R.; Xu, S.-Y.; Chang, G.; Lee, C.-C.; Huang, S.-M.; Wang, B.; Bian, G.; Zheng, H.; Sanchez, D. S.; Belopolski, I.; Alidoust, N.; Neupane, M.; Bansil, A.; Jeng, H.-T.; Lin, H.; Zahid Hasan, M. Prediction of an Arc-Tunable Weyl Fermion Metallic State in MoxW<sub>1-x</sub>Te<sub>2</sub>. *Nat. Commun.* **2016**, *7*, 10639.
- (42) Oliver, S. M.; Beams, R.; Krylyuk, S.; Kalish, I.; Singh, A. K.; Bruma, A.; Tavazza, F.; Joshi, J.; Stone, I. R.; Stranick, S. J.; Davydov, A. V.; Vora, P. M. The Structural Phases and Vibrational Properties of Mo<sub>1-x</sub>W<sub>x</sub>Te<sub>2</sub> Alloys. *2D Mater.* **2017**, *4*, No. 045008.
- (43) Zhou, J.; Liu, F.; Lin, J.; Huang, X.; Xia, J.; Zhang, B.; Zeng, Q.; Wang, H.; Zhu, C.; Niu, L.; Wang, X.; Fu, W.; Yu, P.; Chang, T. R.; Hsu, C. H.; Wu, D.; Jeng, H. T.; Huang, Y.; Lin, H.; Shen, Z.; Yang, C.; Lu, L.; Suenaga, K.; Zhou, W.; Pantelides, S. T.; Liu, G.; Liu, Z. Large-Area and High-Quality 2D Transition Metal Telluride. *Adv. Mater.* **2017**, *29*, 1603471.
- (44) Ma, X.; Guo, P.; Yi, C.; Yu, Q.; Zhang, A.; Ji, J.; Tian, Y.; Jin, F.; Wang, Y.; Liu, K.; Xia, T.; Shi, Y.; Zhang, Q. Raman Scattering in the Transition-metal Dichalcogenides of 1T'-MoTe<sub>2</sub>, Td-MoTe<sub>2</sub>, and Td-WTe<sub>2</sub>. *Phys. Rev. B* **2016**, *94*, 214105.
- (45) Rhodes, D.; Chenet, D. A.; Janicek, B. E.; Nyby, C.; Lin, Y.; Jin, W.; Edelberg, D.; Mannebach, E.; Finney, N.; Antony, A.; Schiros, T.; Klarr, T.; Mazzoni, A.; Chin, M.; Chiu, Y.-C.; Zheng, W.; Zhang, Q. R.; Ernst, F.; Dadap, J. I.; Tong, X.; Ma, J.; Lou, R.; Wang, S.; Qian, T.; Ding, H.; Osgood, R. M., Jr.; Paley, D. W.; Lindenberg, A. M.; Huang, P. Y.; Pasupathy, A. N.; Dubey, M.; Hone, J.; Balicas, L. Engineering the Structural and Electronic Phases of MoTe<sub>2</sub> through W Substitution. *Nano Lett.* **2017**, *17*, 1616.
- (46) Hudie, S. M.; Lee, C.-P.; Mathew, R. J.; Chien, T.-E.; Huang, Y.-J.; Chen, H.-T.; Ho, K. C.; Tseng, C.-A.; Chen, Y.-T. Phase-engineered Weyl Semi-Metallic MoxW<sub>1-x</sub>Te<sub>2</sub> Nanosheets as a Highly Efficient Electrocatalyst for Dye-Sensitized Solar Cells. *Sol. RRL* **2019**, *3*, 1800314.

(47) Dong, S.; Chen, X.; Gu, L.; Zhou, X.; Li, L.; Liu, Z.; Han, P.; Xu, H.; Yao, J.; Wang, H.; Zhang, X.; Shang, C.; Cui, G.; Chen, L. One Dimensional MnO<sub>2</sub>/Titanium Nitride Nanotube Coaxial Arrays for High Performance Electrochemical Capacitive Energy Storage. *Energy Environ. Sci.* **2011**, *4*, 3502–3508.

(48) Qu, J.; Li, G. R.; Gao, X. P. One-Dimensional Hierarchical Titania for Fast Reaction Kinetics of Photoanode Materials of Dye-Sensitized Solar Cells. *Energy Environ. Sci.* **2010**, *3*, 2003–2009.

(49) Ramadoss, A.; Kim, G.-S.; Kim, S. J. Fabrication of Reduced Graphene Oxide/ TiO<sub>2</sub> Nanorod/Reduced Graphene Oxide Hybrid Nanostructures as Electrode Materials for Supercapacitor Applications. *Cryst. Eng. Commun.* **2013**, *15*, 10222–10229.

(50) Mathew, R. J.; Inbaraj, C. R. P.; Sankar, R.; Hudie, S. M.; Nikam, R. D.; Tseng, C.-A.; Lee, C.-H.; Chen, Y.-T. High Unsaturated Room-Temperature Magnetoresistance in Phase-Engineered MoxW<sub>1</sub>-XTe<sub>2</sub>+ $\delta$  Ultrathin Films. *J. Mater. Chem. C* **2019**, *7*, 10996.

(51) Dubrovskii, V. G.; Cirilin, G. E.; Ustinov, V. M. Semiconductor Nanowhiskers: Synthesis Properties and Applications. *Semiconductors* **2009**, *43*, 1539.

(52) Mandl, B.; Stangl, J.; Hilner, E.; Zakharov, A. A.; Hillerich, K.; Dey, A. W.; Samuelson, L.; Bauer, G.; Deppert, K.; Mikkelsen, A. Growth Mechanism of Self-Catalyzed Group III–V Nanowires. *Nano Lett.* **2010**, *10*, 4443–4449.

(53) Hsu, Y.-J.; Lu, S.-Y. Vapor–Solid Growth of Sn Nanowires: Growth Mechanism and Superconductivity. *J. Phys. Chem. B* **2005**, *109*, 4398–4403.

(54) Hou, X.; Wang, X.; Liu, B.; Wang, Q.; Luo, T.; Chen, D.; Shen, G. Hierarchical MnCo<sub>2</sub>O<sub>4</sub> Nanosheet Arrays/Carbon Cloths as Integrated Anodes for Lithium-Ion Batteries with Improved Performance. *Nanoscale* **2014**, *6*, 8858.

(55) Lantz, G.; Laulhé, C.; Ravy, S.; Kubli, M.; Savoini, M.; Tasca, K.; Abreu, E.; Esposito, V.; Porer, M.; Ciavardini, A.; Cario, L.; Rittmann, J.; Beaud, P.; Johnson, S. L. Domain-Size Effects on the Dynamics of a Charge Density Wave in 1T–TaS<sub>2</sub>. *Phys. Rev. B* **2017**, *96*, 224101.

(56) Zou, Y.-C.; Chen, Z.-G.; Liu, S.; Aso, K.; Zhang, C.; Kong, F.; Hong, M.; Matsumura, S.; Cho, K.; Zou, J. Atomic Insights into Phase Evolution in Ternary Transition-Metal Dichalcogenides Nanostructures. *Small* **2018**, *14*, 1800780.

(57) Hussain, S.; Patil, S. A.; Memon, A. A.; Vikraman, D.; Abbas, H. G.; Jeong, S. H.; Kim, H.-S.; Kim, H.-S.; Jung, J. Development of a WS<sub>2</sub>/MoTe<sub>2</sub> Heterostructure as a Counter Electrode for the Improved Performance in Dye-Sensitized Solar Cells. *Inorg. Chem. Front.* **2018**, *5*, 3178–3183.

(58) Sun, K.; Dong, J.; Wang, Z.; Wang, Z.; Fan, G.; Hou, Q.; An, L.; Dong, M.; Fan, R.; Guo, Z. Tunable Negative Permittivity in Flexible Graphene/PDMS Metacomposites. *J. Phys. Chem. C* **2019**, *123*, 23635–23642.

(59) Xie, P.; Li, Y.; Hou, Q.; Sui, K.; Liu, C.; Fu, X.; Zhang, J.; Murugadoss, V.; Fan, J.; Wang, Y.; Fan, R.; Guo, Z. Tunneling-Induced Negative Permittivity in Ni/MnO Nanocomposites by a Bio-Gel Derived Strategy. *J. Mater. Chem. C* **2020**, *8*, 3029–3039.

(60) Sun, K.; Wang, L.; Wang, Z.; Wu, X.; Fan, G.; Wang, Z.; Cheng, C.; Fan, R.; Dong, M.; Guo, Z. Flexible Silver Nanowire/Carbon Fiber Felt Metacomposites with Weakly Negative Permittivity Behavior. *Phys. Chem. Chem. Phys.* **2020**, *22*, 5114–5122.

(61) Syrokostas, G.; Siokou, A.; Leftheriotis, G.; Yianoulis, P. Degradation Mechanisms of Pt Counter Electrodes for Dye Sensitized Solar Cells. *Sol. Energy Mater. Sol. Cells* **2012**, *103*, 119–127.

# Supporting Information

## Stoichiometry-Controlled $\text{Mo}_x\text{W}_{1-x}\text{Te}_2$ Nanowhiskers: A Novel Electro-catalyst for Pt-free Dye-Sensitized Solar Cells

Roshan Jesus Mathew,<sup>†,‡,§,□</sup> Chuan-Pei Lee,<sup>⊥,□</sup> Chi-Ang Tseng,<sup>||</sup> Pradyumna Kumar Chand,<sup>||</sup> Yi-June Huang,<sup>#</sup> Han-Ting Chen,<sup>#</sup> Kuo-Chuan Ho,<sup>#</sup> Aswin kumar Anbalagan,<sup>†</sup> Chih-Hao Lee,<sup>†</sup> and Yit-Tsong Chen<sup>\*,§,||</sup>

<sup>†</sup> Department of Engineering and System Science, National Tsing-Hua University, No. 101, Section 2, Kuang-Fu Road, Hsinchu 30013, Taiwan.

<sup>‡</sup> Nano-Science and Technology Program, Taiwan International Graduate Program, Academia Sinica, No. 128, Section 2, Academia Rd, Nangang, Taipei, 11529, Taiwan.

<sup>§</sup> Institute of Atomic and Molecular Sciences, Academia Sinica, No. 1, Section 4, Roosevelt Road, Taipei 10617, Taiwan.

<sup>⊥</sup> Department of Applied Physics and Chemistry, University of Taipei, Taipei 10048, Taiwan.

<sup>||</sup> Department of Chemistry, National Taiwan University, No. 1, Section 4, Roosevelt Road, Taipei 10617, Taiwan.

<sup>#</sup> Department of Chemical Engineering, National Taiwan University, Taipei 10617, Taiwan.

<sup>□</sup> These authors contributed equally to this work.

\*E-mail: [ytccchem@ntu.edu.tw](mailto:ytccchem@ntu.edu.tw)

## Section S1. Growth of $\text{Mo}_x\text{W}_{1-x}\text{Te}_2$ Nanowhiskers in APCVD Reactions

The synthesis of  $\text{Mo}_x\text{W}_{1-x}\text{Te}_2$  nanowhiskers in APCVD reactions involves three steps: (i) the formation of metal oxychloride at 280 °C, (ii) the decomposition of metal oxychloride and the reduction of metal oxides at 350 °C, and (iii) the tellurization at 760 °C. The temperature profiles during the APCVD synthesis are presented in **Figure S1**. The growth of  $\text{Mo}_x\text{W}_{1-x}\text{Te}_2$  nanowhiskers is highly reproducible.

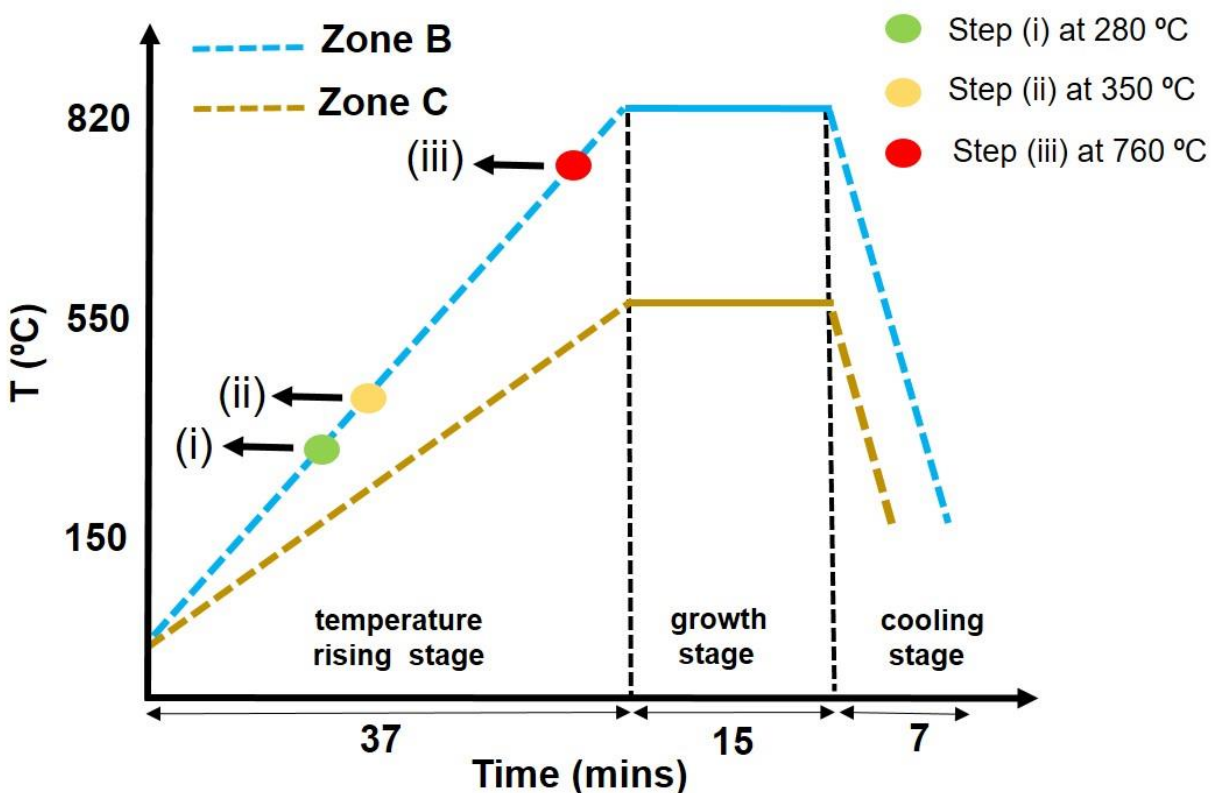


**Figure S1.** The temporal temperature profiles for the synthesis of  $\text{Mo}_x\text{W}_{1-x}\text{Te}_2$  nanowhiskers conducted in APCVD reactions.

## Section S2. Scanning Electron Microscopy (SEM)

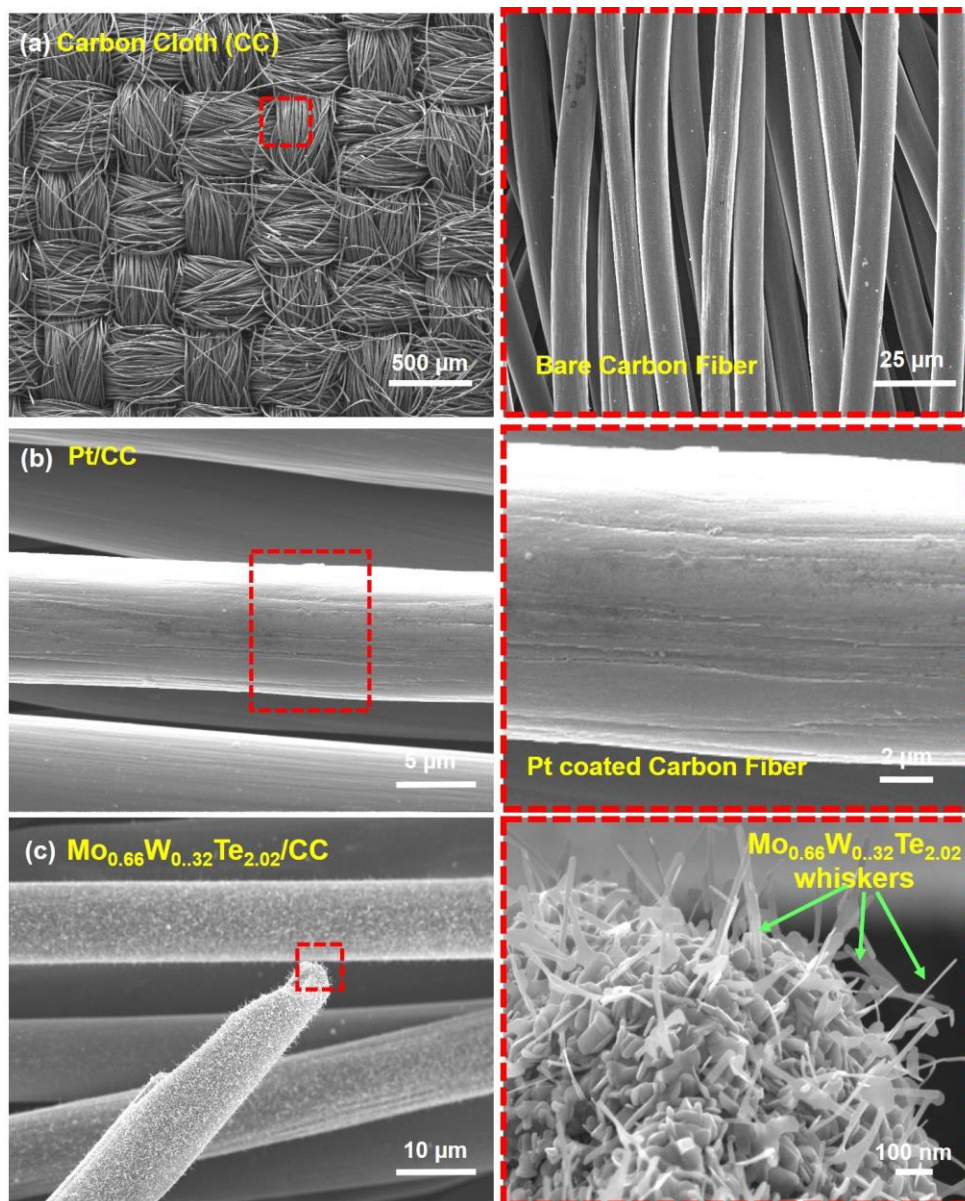


**Figure S2.** SEM images show (a) the bare carbon cloth (CC) surface, (b) carbon fibers coated with platinum (Pt/CC) used as a reference electrode, and (c) carbon fibers decorated with randomly oriented vertical  $\text{Mo}_x\text{W}_{1-x}\text{Te}_2$  nanowhiskers. In the left panels, the regions marked by red dashed squares are magnified in the right panel for detailed morphologies.

### Section S3. X-ray Photoelectron Spectroscopy (XPS)

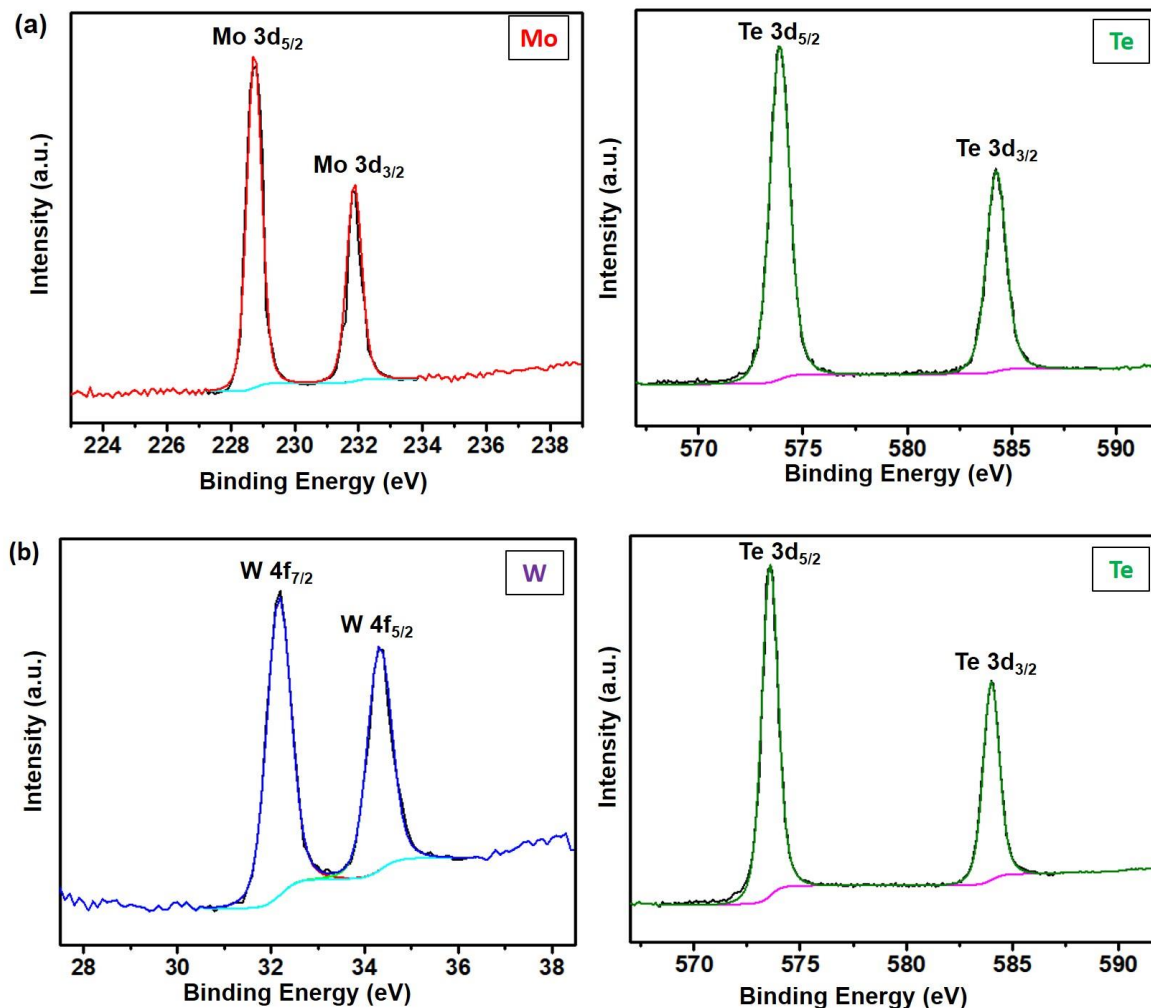


**Figure S3.** The observed XPS spectra of (a) MoTe<sub>2</sub> nanowhiskers and (b) WTe<sub>2</sub> nanowhiskers exhibit the Mo 3d, W 4f, and Te 3d levels, in which the doublets are caused by the spin-orbit couplings. (a) For MoTe<sub>2</sub> nanowhiskers, the binding energies include Mo: 3d<sub>5/2</sub> (228.69 eV) and 3d<sub>3/2</sub> (231.85 eV) and Te: 3d<sub>5/2</sub> (573.60 eV) and 3d<sub>3/2</sub> (583.96 eV). (b) For WTe<sub>2</sub> nanowhiskers, the binding energies observed are W: 4f<sub>7/2</sub> (32.46 eV) and 4f<sub>5/2</sub> (34.65 eV) and Te: 3d<sub>5/2</sub> (573.90 eV) and 3d<sub>3/2</sub> (584.29 eV).

## Section S4. High-Resolution Transmission Electron Microscopy (HR-TEM)

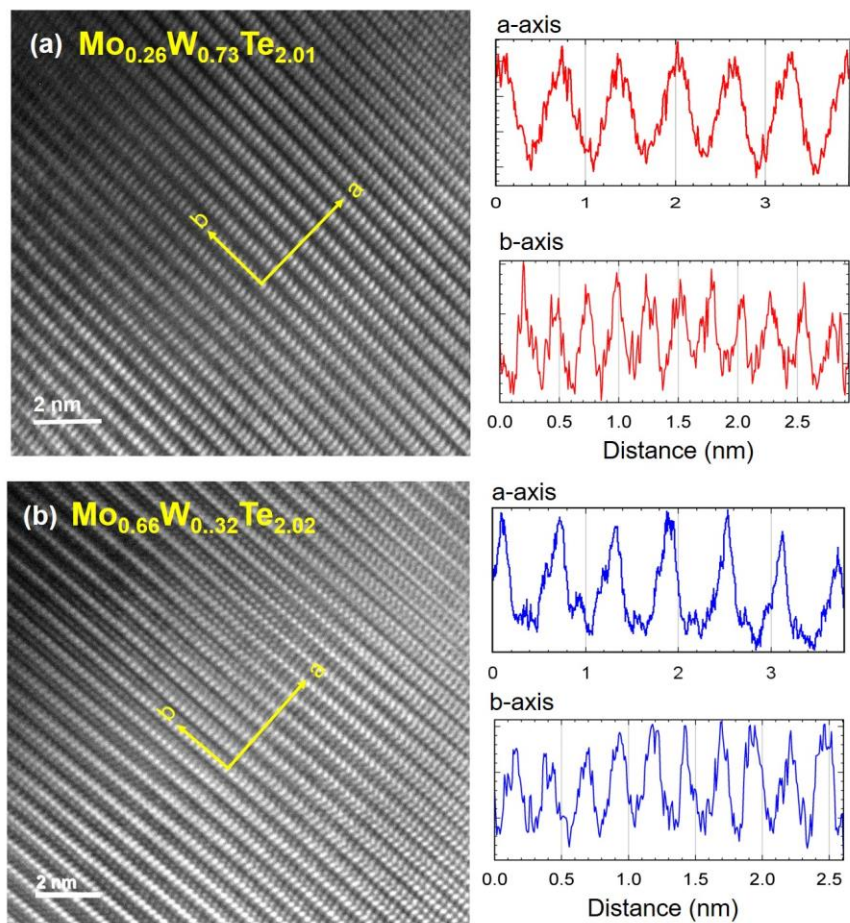


**Figure S4.** In the left column, the HR-TEM images of (a)  $T_d\text{-Mo}_{0.26}\text{W}_{0.73}\text{Te}_{2.01}$  and (b)  $IT'\text{-} \& T_d\text{-Mo}_{0.66}\text{W}_{0.32}\text{Te}_{2.02}$  nanowiskers are presented. In the right column, the plot profiles shown in the panels reveal the lattice spacings along the a-axis (top) and b-axis (bottom) of the crystalline structures in the HR-TEM images.

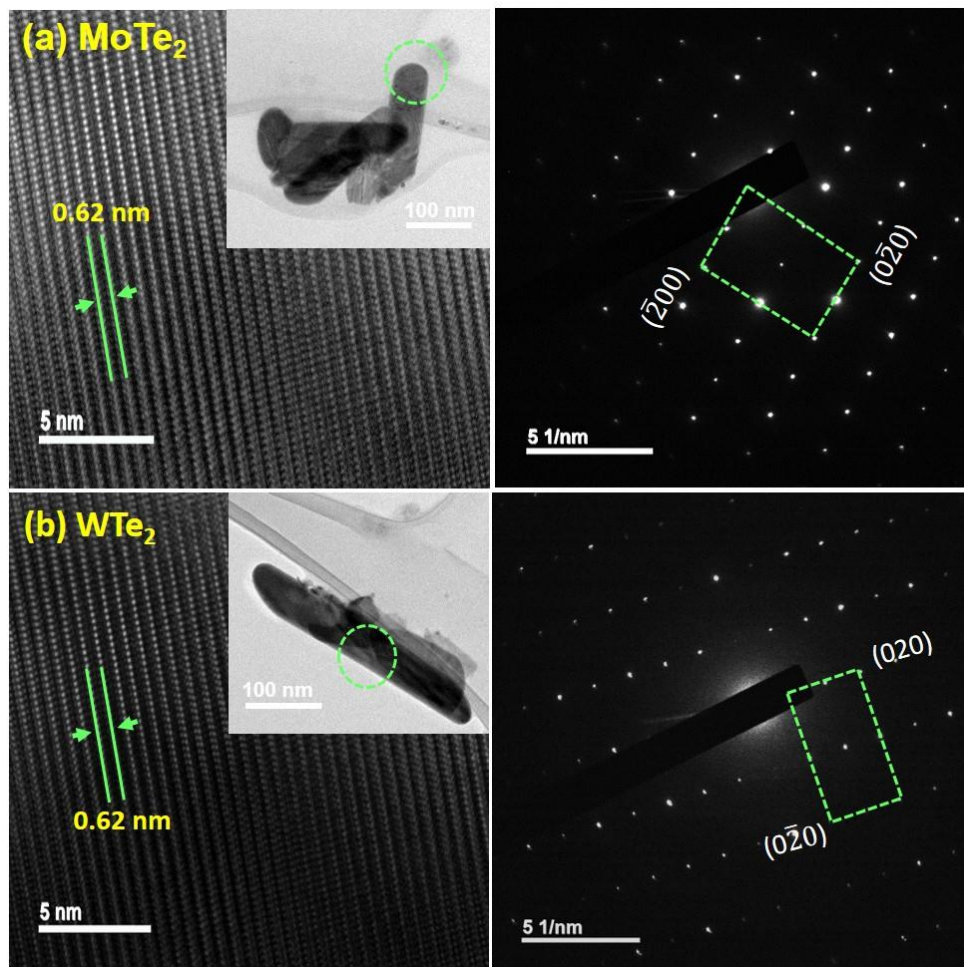


**Figure S5.** The HR-TEM images and SAED patterns of (a) a MoTe<sub>2</sub> nanowhisker and (b) a WTe<sub>2</sub> nanowhisker were obtained. A TEM image of the single nanowhisker for taking the HR-TEM and SAED examinations is presented in the inset, where the spot marked by a green circle was selected for the HR-TEM and SAED measurements.

## Section S5. Electrochemical Experiments

### 1. Materials and Chemicals

Lithium iodide (LiI, synthetical grade) and iodine (I<sub>2</sub>, synthetical grade) were obtained from Merck. Acetone (99+%), tert-butyl alcohol (tBA, 96%), guanidine thiocyanate (GuSCN, 99+%), and 4-tert-butylpyridine (TBP, 96%) were bought from Acros. Titanium(IV) tetraisopropoxide (TTIP, >98%), lithium perchlorate (LiClO<sub>4</sub>, ≥98.0%), ethanol (EtOH, absolute), isopropyl alcohol (IPA, 99.5%), sulfuric acid (H<sub>2</sub>SO<sub>4</sub>, 95–97%), and 2-methoxyethanol (99.95%) were received from Sigma-Aldrich. Acetonitrile (ACN, 99.99%) was procured from J. T. Baker. 1,2-dimethyl-3-propylimidazolium iodide (DMPII) and cis-diisothiocyanato-bis (2,2'-bipyridyl-4,4'-dicarboxylato) ruthenium(II) bis(tetra-butylammonium) (N719 dye) were purchased from Solaronix (S.A., Aubonne, Switzerland). Carbon cloth (CC, W0S1002, thickness: 0.36 mm, basic weight: 120 g cm<sup>-2</sup>, sheet resistance: 0.63 Ω sq.<sup>-1</sup>) was obtained from CeTech Co., Ltd., Taiwan.

### 2. Preparation of Counter Electrodes and Electrochemical Measurements

The as-grown Mo<sub>x</sub>W<sub>1-x</sub>Te<sub>2</sub>/CCs with various stoichiometric ratios were used as different counter electrodes (CEs) in a DSSC for tests. Meanwhile, with a direct current (DC) sputtering method, a Pt catalytic layer deposited on a cleaned CC substrate was used as a standard CE (represented by a sputtered Pt/CC).

The surface of the DSSC was covered by a mask, leaving a light-illuminating area of 0.16 cm<sup>2</sup>, and then illuminated by a class-A quality solar simulator (XES-301S, AM 1.5G, SAN-EI ELECTRIC CO., LTD.) with the light intensity of 100 mW cm<sup>-2</sup>. Incident light intensity (100 mW cm<sup>-2</sup>) was calibrated with a standard Si cell (PECSI01, Peccell Technologies, Inc.). Photoelectrochemical characteristics of the DSSC were recorded with a potentiostat/galvanostat

(PGSTAT 30, Autolab, Eco-Chemie, Netherlands). The incident photon-to-electron conversion efficiency (IPCE) curves were obtained at the short-circuit condition. The light source was a class-A quality solar simulator (PEC-L11, AM1.5G, Peccell Technologies, Inc.) and the light was focused through a monochromator (74100, Oriel Instrument) onto the photovoltaic cell. Then, the IPCE ( $\lambda$ ) can be calculated by using the equation,  $\text{IPCE}(\lambda) = 1240 (J_{\text{SC}}/\lambda\phi)$ , in which  $\lambda$  is the wavelength,  $J_{\text{SC}}$  is the short-circuit photocurrent density ( $\text{mA cm}^{-2}$ ) recorded with a potentiostat/galvanostat, and  $\phi$  is the incident radiative flux ( $\text{W m}^{-2}$ ) measured with an optical detector (818-SL, Newport) and a power meter (1916-R, Newport).

CV was performed to investigate the electrocatalytic abilities of the tested CEs. The CV was carried out with a three-electrode electrochemical system (a close system) using one of the tested samples (i.e., bare CC,  $\text{Mo}_x\text{W}_{1-x}\text{Te}_2/\text{CC}$ , and a sputtered Pt/CC) as the working electrode, a Pt foil as the CE, and a  $\text{Ag}/\text{Ag}^+$  electrode as the reference electrode in an acetonitrile (ACN) solution, containing 10 mM  $\text{I}^-$ , 1 mM  $\text{I}_2$ , and 0.1 M  $\text{LiClO}_4$ .

Electrochemical properties of the tested CEs were also quantified by Tafel polarization curves (Tafel curves) and EIS, where a symmetric cell, consisting of the same catalytic film on both anode and cathode, was used for these measurements. The data were recorded by the abovementioned potentiostat/galvanostat equipped with a FRA2 module. The electrolyte, containing 0.1 M LiI, 0.6 M DMPII, 0.05 M  $\text{I}_2$ , and 0.5 M TBP in 3-methoxypropionitrile (MPN)/ acetonitrile (ACN) (volume ratio of 1/1), was used for the Tafel analysis (with a scan rate of  $50 \text{ mV s}^{-1}$ ) and EIS measurements. Under the open-circuit condition, the EIS analysis was performed between 10 mHz and 65 kHz with an AC amplitude of  $\pm 10 \text{ mV}$ .

## Section S6. Comparison of Electrocatalytic Performance

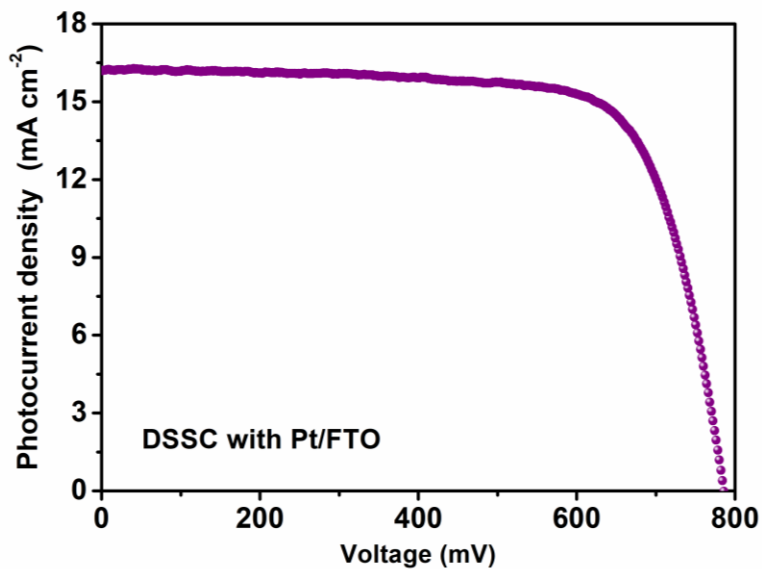


**Figure S6.** The photocurrent density-voltage ( $J$ - $V$ ) measurement of a DSSC with a Pt/FTO CE was conducted under AM 1.5G illumination at  $100 \text{ mW cm}^{-2}$ .

**Table S1.** The photovoltaic parameters of a Pt/FTO counter electrode

Counter Electrode	$\eta$ (%)	$V_{oc}$ (mV)	$J_{sc}$ ( $\text{mA cm}^{-2}$ )	$FF$
Pt/FTO	9.43	784	16.21	0.74

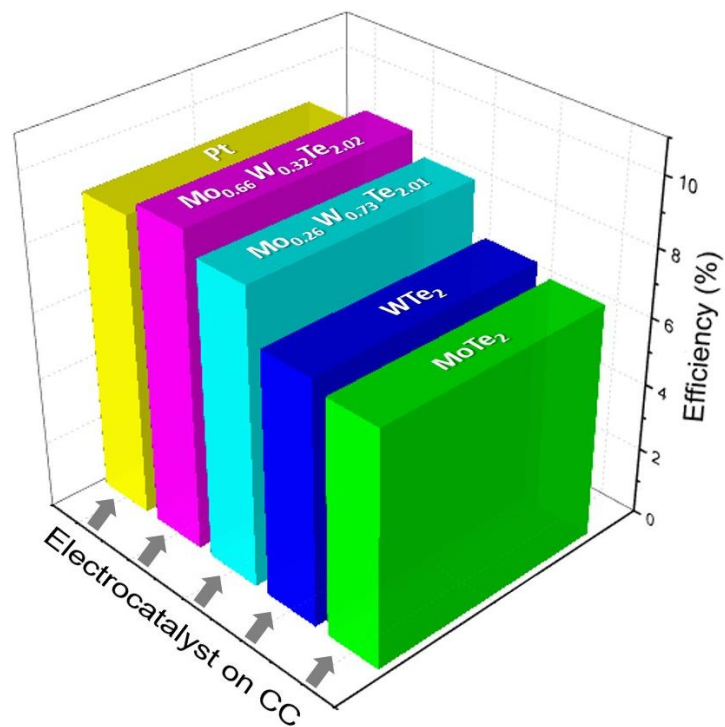


**Figure S7.** The electrocatalytic efficiencies of different stoichiometric  $\text{Mo}_x\text{W}_{1-x}\text{Te}_2/\text{CCs}$  used as CEs in a DSSC are listed for comparison.

## Section S7. Reproducibility Test

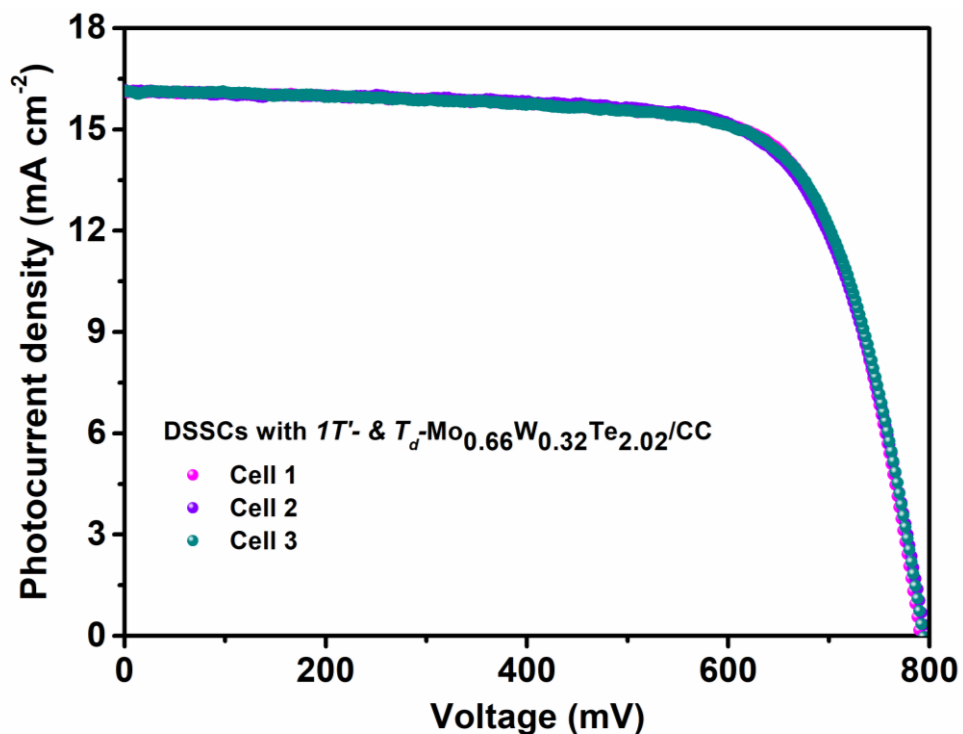


**Figure S8.** The photocurrent density-voltage ( $J$ - $V$ ) measurements of three different  $IT'$ - &  $T_d'$ - $Mo_{0.66}W_{0.32}Te_{2.02}/CC$  CE-based DSSCs were conducted under AM 1.5G illumination at  $100 \text{ mW cm}^{-2}$  to demonstrate the reproducibility of the material under study.

**Table S2.** The reproducibility test of  $IT'$ - &  $T_d'$ - $Mo_{0.66}W_{0.32}Te_{2.02}/CC$  CE-based DSSCs

$IT'$ - & $T_d'$ - $Mo_{0.66}W_{0.32}Te_{2.02}/CC$ CE-based DSSCs	$\eta$ (%)	$V_{oc}$ (mV)	$J_{sc}$ ( $mA \text{ cm}^{-2}$ )	$FF$
Cell 1	9.38	790	16.13	0.74
Cell 2	9.28	794	16.15	0.72
Cell 3	9.33	792	16.14	0.73
Average	$9.33 \pm 0.05$	$792 \pm 2$	$16.14 \pm 0.01$	$0.73 \pm 0.01$

## Section S8. Long-Term Stability Tests

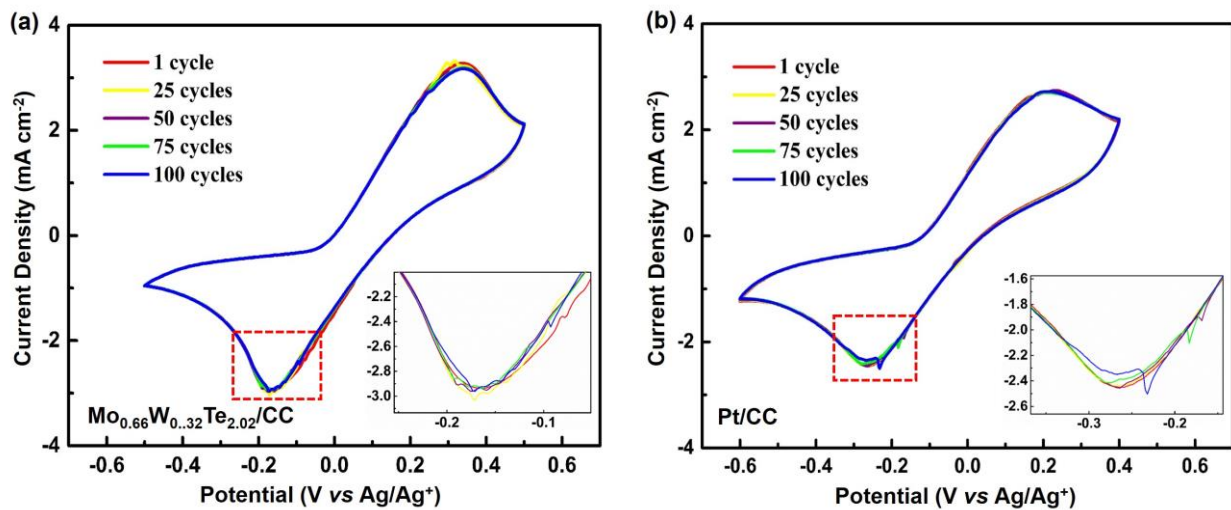


**Figure S9.** The stability tests of the CEs fabricated with (a)  $IT'$ - &  $T_d$ -Mo<sub>0.66</sub>W<sub>0.32</sub>Te<sub>2.02</sub>/CC and (b) Pt/CC were conducted by continuous 100-cycle CV measurements in the  $I^-/I_3^-$  redox reaction. The regions marked by red dashed squares are magnified in the insets.

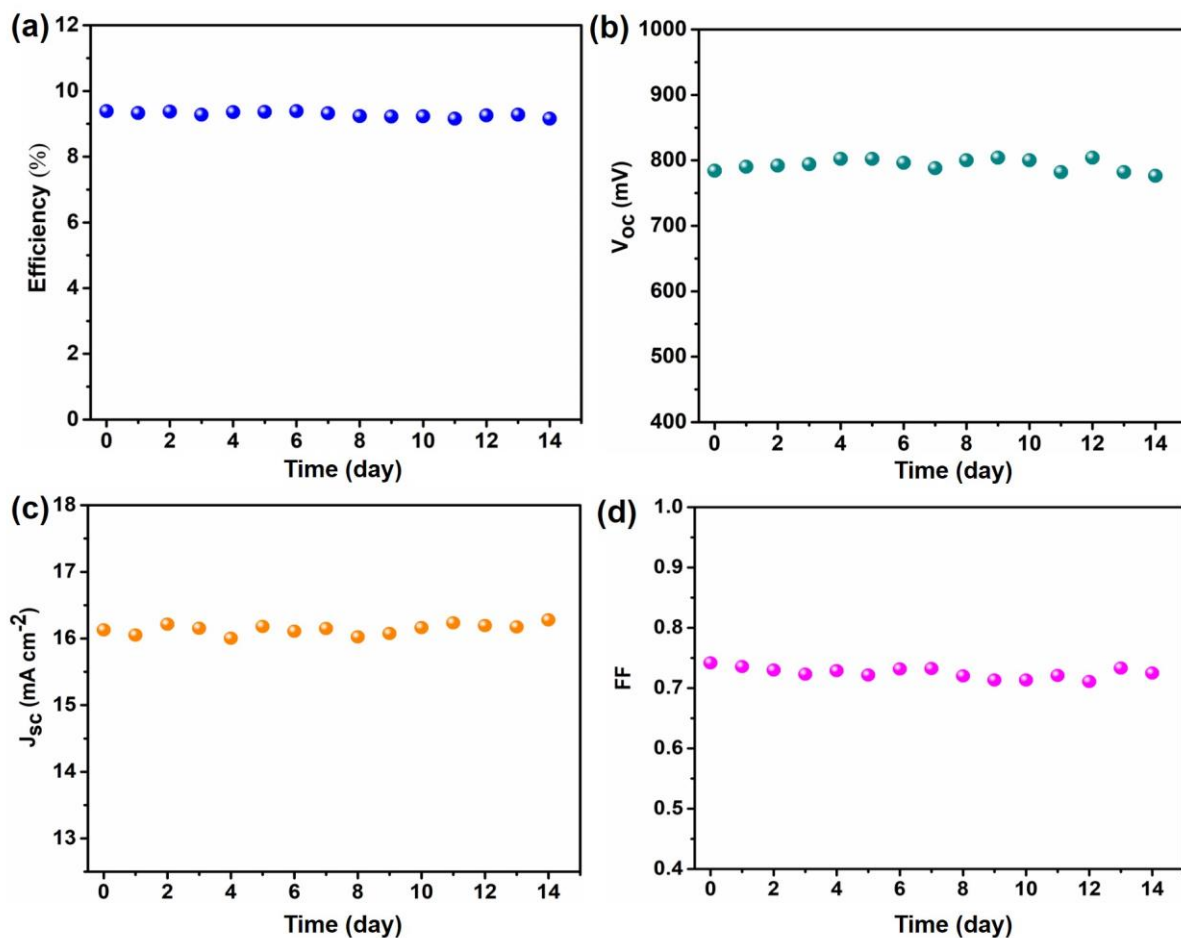


**Figure S10.** The long-term stability of the DSSC fabricated with a  $IT'$ - &  $T_d$ - $\text{Mo}_{0.66}\text{W}_{0.32}\text{Te}_{2.02}/\text{CC}$  CE was tested for 15 days to demonstrate the stability of the photovoltaic parameters of (a) efficiency ( $\eta$ ), (b) open-circuit voltage ( $V_{oc}$ ), (c) short-circuit photocurrent density ( $J_{sc}$ ), and (d) fill factor ( $FF$ ). In this test, the cell was sealed simultaneously with Surllyn and epoxy glue. The cell efficiency was measured once per day after storing the cell in a dark condition at room temperature.

## Section S9. Comparison of Photovoltaic Parameters

**Table S3.** The measured photovoltaic parameters of the DSSCs with various TMDs-based CEs

<b>Counter Electrodes</b>	$J_{sc}$ ( $\text{mAcm}^{-2}$ )	$V_{oc}$ (V)	$FF$ (%)	$R_{ct}$ ( $\Omega \text{ cm}^2$ )	$\eta$ (%)	<b>Ref.</b>
MoS <sub>2</sub> /NGr	15.36	0.77	66	16.73	7.82	S1
WS <sub>2</sub> /MWCNTs	13.63	0.75	72	2.49	7.36	S2
TiS <sub>2</sub> /graphene hybrid	17.76	0.72	68.5	0.63	8.80	S3
NiS <sub>2</sub> /RGO	16.55	0.749	69	2.9	8.55	S4
FeS <sub>2</sub>	15.20	0.79	65	-	7.97	S5
CoS <sub>2</sub>	14.62	0.71	64	7.21	6.78	S6
SnS <sub>2</sub> /C	17.47	0.745	61.9	5.2	8.06	S7
MoSe <sub>2</sub>	16.71	0.746	72.2	1.39	9.00	S8
NbSe <sub>2</sub> /C	15.58	0.77	65	3.52	7.80	S9
WSe <sub>2</sub>	15.50	0.73	66	0.78	7.48	S10
TaSe <sub>2</sub>	15.81	0.73	64	1.89	7.32	S10
NiSe <sub>2</sub>	15.94	0.734	74.3	0.81	8.69	S11
FeSe <sub>2</sub>	16.14	0.744	70	0.49	8.39	S12
CoSe <sub>2</sub> /C	18.16	0.76	71	-	9.87	S13
Bi <sub>2</sub> Se <sub>3</sub> /graphene	16.36	0.75	57	-	7.09	S14

WS <sub>2</sub> /MoTe <sub>2</sub>	15.34	0.74	69.69	3.98	7.99	S15
MoTe <sub>2</sub>	16.00	0.69	65.64	25.97	7.25	S16
<b><i>IT'</i>- &amp; <i>T<sub>d</sub></i>-Mo<sub>0.66</sub>W<sub>0.32</sub>Te<sub>2.02</sub></b>	<b>16.29</b>	<b>0.788</b>	<b>73</b>	<b>0.62</b>	<b>9.40</b>	<b>This work</b>

In **Table S3**, the photovoltaic parameters of the DSSCs with various TMDs-fabricated CEs were listed to compare with those of a *IT'*- & *T<sub>d</sub>*-Mo<sub>0.66</sub>W<sub>0.32</sub>Te<sub>2.02</sub>/CC CE-based DSSC. The photovoltaic parameters include short-circuit photocurrent density ( $J_{sc}$ ), open-circuit voltage ( $V_{oc}$ ), fill factor ( $FF$ ), charge-transfer resistance ( $R_{ct}$ ), and power conversion efficiency ( $\eta$ ). All measurements were conducted in the I<sub>3</sub><sup>-</sup>/I redox couple with N719 photosensitizer dye. As can be seen in the Table, the *IT'*- & *T<sub>d</sub>*-Mo<sub>0.66</sub>W<sub>0.32</sub>Te<sub>2.02</sub>/CC CE-based DSSC possesses small charge-transfer resistance to enhance the efficiency of 9.4% (despite slightly less than 9.87% of the CoSe<sub>2</sub>/C hybrid). The comparative analysis demonstrates that the *IT'*- & *T<sub>d</sub>*-Mo<sub>0.66</sub>W<sub>0.32</sub>Te<sub>2.02</sub>/CC CE of small charge-transfer resistance can be used in DSSCs to improve electrocatalytic activity.

## References

- S1. Fan, M. S.; Lee, C. P.; Li, C. T.; Huang, Y. J.; Vittal, R.; Ho, K. C. Nitrogen-Doped Graphene/Molybdenum Disulfide Composite as the Electrocatalytic Film for Dye Sensitized Solar Cells. *Electrochim. Acta*, **2016**, *211*, 164–172.
- S2. Wu, J.; Yue, G.; Xiao, Y.; Huang, M.; Lin, J.; Fan, L.; Lan, Z.; Lin, J. Y. Glucose Aided Preparation of Tungsten Sulfide/ Multi-Wall Carbon Nanotube Hybrid and Use as Counter Electrode in Dye-Sensitized Solar Cells. *ACS Appl. Mater. Interface*, **2012**, *4*, 6530–6536.
- S3. Meng, X.; Yu, C.; Lu, B.; Yang, J.; Qiu, J.; Dual Integration System Endowing Two-Dimensional Titanium Disulfide with Enhanced Triiodide Reduction Performance in Dye-Sensitized Solar Cells. *Nano Energy*, **2016**, *22*, 59–69.
- S4. Li, Z.; Gong, F.; Zhou, G.; Wang, Z. S. NiS<sub>2</sub>/Reduced Graphene Oxide Nanocomposites for Efficient Dye-Sensitized Solar Cells. *J. Phys. Chem. C*, **2013**, *117*, 6561– 6566.
- S5. Shukla, S.; Loc, N. H.; Boix, P. P.; Koh, T. M.; Prabhakar, R. R.; Mulmudi, H. K.; Zhang, J.; Chen, S.; Ng, C. F.; Huan, C. H. A.; Mathews, N. Iron Pyrite Thin Film Counter Electrodes for Dye-Sensitized Solar Cells: High Efficiency for Iodine and Cobalt Redox Electrolyte Cells. *ACS Nano*, **2014**, *8*, 10597– 10605.
- S6. Jin, J.; Zhang, X.; He, T. Self-Assembled CoS<sub>2</sub> Nanocrystal Film as an Efficient Counter Electrode for Dye-Sensitized Solar Cells. *J. Phys. Chem. C*, **2014**, *118*, 24877–24883.
- S7. Bai, Y.; Zong, X.; Yu, H.; Chen, Z. G.; Wang, L. Scalable Low-Cost SnS<sub>2</sub> Nanosheets as Counter Electrode Building Blocks for Dye-Sensitized Solar Cells. *Chem.–Eur. J.*, **2014**, *20*, 8670–8676.
- S8. Lee, L. T. L.; He, J.; Wang, B.; Ma, Y.; Wong, K. Y.; Li, Q.; Xiao, X.; Chen, T. Few-Layer MoSe<sub>2</sub> Possessing High Catalytic Activity Towards Iodide/Tri-Iodide Redox Shuttles. *Sci. Rep.*, **2014**, *4*, 4063–4069.

- S9. Guo, J.; Shi, Y.; Zhu, C.; Wang, L.; Wang, N.; Ma, T. Cost Effective and Morphology-Controllable Niobium Diselenides for Highly Efficient Counter Electrodes of Dye Sensitized Solar Cells. *J. Mater. Chem. A*, **2013**, *1*, 11874–11879.
- S10. Guo, J.; Liang, S.; Shi, Y.; Hao, C.; Wang, X.; Ma, T. Transition Metal Selenides as Efficient Counter-Electrode Materials for Dye-Sensitized Solar Cells. *Phys. Chem. Chem. Phys.*, **2015**, *17*, 28985–28992.
- S11. Gong, F.; Xu, X.; Li, Z.; Zhou, G.; Wang, Z. S. NiSe<sub>2</sub> as an Efficient Electrocatalyst for a Pt-Free Counter Electrode of Dye-Sensitized Solar Cells. *Chem. Commun.*, **2013**, *49*, 1437–1439.
- S12. Huang, S.; He, Q.; Chen, W.; Zai, J.; Qiao, Q.; Qian, X. 3D Hierarchical FeSe<sub>2</sub> Microspheres: Controlled Synthesis and Applications in Dye-Sensitized Solar Cells. *Nano Energy*, **2015**, *15*, 205–215.
- S13. Chiu, I. T.; Li, C. T.; Lee, C. P.; Chen, P. Y.; Tseng, Y. H.; Vittal, R.; Ho, K. C. Nanoclimbing-Wall-Like CoSe<sub>2</sub>/ Carbon Composite Film for the Counter Electrode of a Highly Efficient Dye-Sensitized Solar Cell: A Study on the Morphology Control. *Nano Energy*, **2016**, *22*, 594–606.
- S14. Zhu, L.; Cho, K. Y.; Oh, W. C. Microwave-Assisted Synthesis of Bi<sub>2</sub>Se<sub>3</sub>/Reduced Graphene Oxide Nanocomposite as Efficient Catalytic Counter Electrode for Dye-Sensitized Solar Cell. *Fullerenes, Nanotubes, Carbon Nanostruct.*, **2016**, *24*, 622–629.
- S15. Hussain, S.; Patil, S. A.; Memon, A. A.; Vikraman, D.; Abbas, H. G.; Jeong, S. H.; Kim, H.-S.; Kim, H.-S.; Jung, J. Development of a WS<sub>2</sub>/MoTe<sub>2</sub> Heterostructure as a Counter Electrode for the Improved Performance in Dye-Sensitized Solar Cells. *Inorg. Chem. Front.* **2018**, *5*, 3178-3183.

S16. Hussain, S.; Patil, S. A.; Vikraman, D.; Mengal, N.; Liu, H.; Song, W.; An, K.-S.; Jeong, S. H.; Kim, H.-S.; Jung, J. Large Area Growth of MoTe<sub>2</sub> Films as High Performance Counter Electrodes for Dye-Sensitized Solar Cells. *Sci. Rep.* **2018**, *8*, 29.